



Eidgenössische Technische Hochschule Zürich  
Swiss Federal Institute of Technology Zurich

PAUL SCHERRER INSTITUT



# Quantitative Phase-Contrast Imaging and Breast-Tissue Decomposition

Semester Thesis

Javier García Baroja

garciaja@student.ethz.ch

**Affiliation:**

X-ray Tomography Group  
ETH Zürich, Paul Scherrer Institute

**Supervision:**

Supervisor

Prof. Dr. Marco Stampanoni

Adviser

Dr. Michał Rawlik

June 6, 2022

*- This page was intentionally left blank -*

# Abstract

Breast cancer is, in absolute terms, the most common type of cancer. Although screening programs notably reduce mortality, it accounts for one sixth of all cancer related deaths, equivalent to 690,000 annually.

The existing diagnostic methods are flawed as a result of their invasive nature, cost, or radiation dose, among other reasons. X-ray imaging is the most widely used modality for breast cancer diagnosis and screening. However, the current techniques only make use of absorption contrast, which is not ideally suited for soft tissue imaging.

Talbot-Lau grating interferometry (GI) provides both attenuation and phase-contrast (PC). Consequently, phase conveys additional contrast information to absorption that can complement it as a diagnostic tool for mammography.

However, the large amount of data generated by this approach may turn into a short-coming by adding pressure to the already saturated radiology departments. This creates the need for computational tools that facilitate diagnosis and prognosis, and makes it crucial that analysis tools are developed in parallel to new imaging methods.

The present semester thesis is framed around the development of such computer aided diagnosis (CAD) tools. The goal is to implement material decomposition on the Talbot-Lau GI images to yield lipid, protein and water content. These masks carry key information for diagnosis, given that tumors show a different composition from their surroundings.

This work proposes a method for material decomposition. The results show that the imaging system is quantitative, which enables successful decomposition, and at the same time, that artifacts play a substantial role in the correct functioning of this approach.

Therefore, despite the satisfactory outcome, further investigation is required to unveil what the sources of the system's artifacts are and how to correct them without losing the quantitative quality it produces.

**Keywords:** breast imaging, X-ray imaging, phase contrast, grating interferometry, computer aided diagnosis, material decomposition.

*- This page was intentionally left blank -*

# Acknowledgments

Pursuing this semester thesis has been one of my best decisions so far at ETH. Not only for how much it has taught me from an academic perspective but also for the people it has enabled me to meet along this journey.

I would like to start by thanking all the members of the *bunker's team* for their suggestions and the many interesting conversations. I would also like to extend my gratitude to the rest of the TOMCATs for their warm welcome to a temporary student.

More specifically, I would also want to thank Michał, my adviser for this work. Thank you for your support, for fostering my curiosity for the project, and for the injection of motivation that our chats meant.

I cannot think of a better place where I could have completed my semester project, so I would finally like to thank Professor Marco Stampanoni for granting me the chance to join the team for this enriching and unforgettable experience.

Javier García Baroja  
Zürich, June 2022

*- This page was intentionally left blank -*

# Table of Contents

<b>Abstract</b>	<b>ii</b>
<b>Acknowledgments</b>	<b>iv</b>
<b>1 Introduction</b>	<b>1</b>
<b>2 Background</b>	<b>3</b>
2.1 X-ray imaging . . . . .	3
2.1.1 Interaction of X-rays with matter . . . . .	3
2.1.2 Complex index of refraction . . . . .	4
2.2 Grating interferometry . . . . .	6
2.2.1 Hardware and working principles . . . . .	6
2.3 X-ray tomography . . . . .	8
2.3.1 Computed Tomography . . . . .	8
2.3.2 Reconstruction in grating interferometry . . . . .	9
2.3.3 Artifacts in tomography . . . . .	12
2.4 Material decomposition . . . . .	12
2.4.1 Using dual energy absorption imaging . . . . .	13
2.4.2 Using phase and absorption imaging . . . . .	13
<b>3 Materials</b>	<b>14</b>
3.1 Static set-up . . . . .	14
3.2 Phantom properties . . . . .	14
3.3 Meat properties . . . . .	15
3.4 Software . . . . .	16
<b>4 Methods</b>	<b>17</b>
4.1 Sample preparation and scanning . . . . .	17
4.2 System assessment . . . . .	19
4.2.1 Calculation of retrieved values . . . . .	19

<i>TABLE OF CONTENTS</i>	vii
4.2.2 Calculation of effective energies and theoretical values . . . . .	19
4.2.3 Measurement of precision . . . . .	20
4.3 Material decomposition . . . . .	20
<b>5 Results and Discussion</b>	<b>22</b>
5.1 Image acquisition . . . . .	22
5.2 System assessment . . . . .	22
5.2.1 Calculated values . . . . .	22
5.2.2 Analysis of results . . . . .	24
5.3 Material decomposition . . . . .	25
5.4 Limitations and future work . . . . .	27
<b>6 Conclusions</b>	<b>29</b>
<b>Bibliography</b>	<b>30</b>
<b>A Supporting results figures</b>	<b>A-1</b>
A.1 Acquisition . . . . .	A-5
A.2 System assessment . . . . .	A-5
A.3 Material decomposition . . . . .	A-5

*- This page was intentionally left blank -*

# List of Figures

2.1	Soft tissue mass attenuation coefficient as function of energy . . . . .	4
2.2	X-ray absorption and phase shift after a change of medium . . . . .	6
2.3	X-ray grating Interferometer . . . . .	7
2.4	Signal Retrieval in Talbot-Lau Interferometer . . . . .	8
2.5	The geometry of lines and projections . . . . .	8
2.6	Projection geometry for phase signal . . . . .	11
3.1	Grating Interferometer geometry . . . . .	14
3.2	Scanned phantoms . . . . .	15
3.3	Scanned bacon piece . . . . .	16
4.1	Flat field phase map of the grating interferometer . . . . .	19
5.1	Center slice of acquired volumes . . . . .	23
5.2	Scatter plot $\mu$ and $\delta$ . . . . .	26
5.3	Material decomposition applied to bacon sample . . . . .	27
A.1	Phantom 1 profiles in z-direction . . . . .	A-1
A.2	Phantom 2 profiles in z-direction . . . . .	A-2
A.3	Phantom 1 histogram by materials . . . . .	A-3
A.4	Phantom 2 histogram by materials . . . . .	A-4
A.5	Distribution of $\mu$ and $\delta$ values in the bacon sample reconstruction . . . . .	A-5

*- This page was intentionally left blank -*

# List of Tables

3.1	Composition of phantom elements . . . . .	15
3.2	Composition of lipids and proteins . . . . .	16
5.1	Phantom 1 attenuation and refractive decrement . . . . .	24
5.2	Phantom 2 attenuation and refractive decrement . . . . .	24
5.3	Relative uncertainty and errors . . . . .	25

*- This page was intentionally left blank -*

# List of Abbreviations

<b>2D</b>	two-dimensional
<b>3D</b>	three-dimensional
<b>CT</b>	computed tomography
<b>CAD</b>	computer aided diagnosis
<b>DABAX</b>	database for X-ray applications
<b>EM</b>	electromagnetic radiation
<b>FBP</b>	filtered back-projection
<b>FT</b>	Fourier transform
<b>GI</b>	grating interferometry
<b>IFT</b>	inverse Fourier transform
<b>MRI</b>	magnetic resonance imaging
<b>NIST</b>	National Institute of Standards and Technology
<b>PC</b>	phase-contrast
<b>PMMA</b>	polymethyl methacrylate
<b>POM</b>	polyoxymethylene
<b>PSI</b>	Paul Scherrer Institut

*- This page was intentionally left blank -*

# Introduction

---

Breast cancer is the most common cancer and the leading cause of cancer mortality for women worldwide, accounting for one in every six cancer-related deaths [1]. In Europe, the 5-year survival rate for females aged 47 to 54 (the height of diagnostic risk [1]) is 82.9% [2].

The statistics above underline the global interest in early detection of breast cancer. Developed countries have X-ray mammography screening programs in place that effectively reduce the rate of advanced breast cancer by 25%, as shown by S. W. Duffy et al. [3]. However, they have clear deficiencies, indicated by a false positive rate higher than 20% [4] for screening that originates in the breast morphology itself or the limitations of the imaging techniques. False negatives especially arise in dense-breast patients and are detrimental because they transmit a false sense of security for the patient that can have fatal consequences [5]. Finally, the screening programs show a risk of over-diagnosis of 23% [6].

X-ray imaging is the gold-standard in screening programs but it is not the only approach to breast cancer detection. Other modalities are also employed, but all have specific drawbacks, whether cost (microwave imaging, magnetic resonance imaging (MRI)), high radiation dose (nuclear imaging) or spatial resolution (ultrasound) [7].

In any case, the X-ray imaging options are not perfectly suited either. Traditional mammography only provides two-dimensional (2D) information, hindering localization [8]. Digital breast tomosynthesis, despite its improved performance, is still unable to produce sharp images. Although breast computed tomography (CT) produces three-dimensional (3D) reconstruction without breast compression, it is limited by the weak absorption contrast of soft tissue which stems from the fact that it has low absorption coefficients and consequently an intrinsically low absorption signal [9]. Hence the need for a more appropriate method prevails.

The contrast in X-ray images discussed thus far results from the various amount of absorption of the X-rays. This is not the only possibility: the refraction when an incident X-ray beam penetrates an object can also be used for imaging [10]. In fact, it has been shown that PC overcomes absorption in the typical energy range of mammography [11].

Talbot-Lau GI uses a clinical X-ray source and three lamella-like gratings. The Talbot effect is created by a grating with parallel lamellas that forces a periodic phase shift on the beam, resulting in a self-image of a periodic intensity pattern of parallel lines downstream. The pattern will be distorted by coherent refraction of the sample, while small-angle scattering will blur it. These two and the attenuation signal are sensed, which explains why this approach is promising as a solution for the shortcomings of breast imaging.

On a different note, it stands to reason that although moving to this type of imaging holds great potential, the vast amount of information would intensify the pressure experienced by the already saturated radiology departments [12]. The large amount of data along with the shortage of radiologists is motivating the development of CAD systems [13].

The data must be quantitative in order for these approaches to be easily transferable across patients and systems. Such is the case with Talbot-Lau GI imaging, which retrieves the distribution of attenuation coefficients and refractive index decrements [14]. In the energy range of mammography, PC and attenuation information are complementary and allow for material decomposition into water, lipid and protein content [15]. This separability is of clinical relevance because tumors have a distinct composition compared to their surroundings [16].

The purpose of this study is to provide such a tool. This work implements an assessment of the precision of the current imaging set-up and a method for the material decomposition as a way to facilitate tumor detection and diagnosis.

This work has been performed at the *X-ray Tomography Group*, part of the *Paul Scherrer Institut (PSI)*, in collaboration with the adviser of the project.

In particular, the author has been responsible for the data pre-processing and preparation, method implementation, and evaluation of the results.

The remainder of this thesis is organized into the following chapters. Chapter 2 covers the theoretical background on X-ray imaging and reconstruction and briefly describes the state-of-the-art in material decomposition. Chapters 3 and 4 detail the material and methodologies followed throughout the project. Chapter 5 discloses the results and provides discussion as well as an evaluation of the current limitations, followed by a summary of the main outcomes in chapter 6.

# Background

---

This chapter provides the necessary theoretical basis to understand the design of the project and the results it yields.

## 2.1 X-ray imaging

X-rays are a form of high energy electromagnetic radiation (EM) with a wavelength in the Ångström ( $10^{-10}$  m) scale [17]. From the moment of their discovery by Wilhelm C. Röntgen in 1895 [18], their higher penetration capability has fueled their use in a number of sectors (medicine, crystallography, security, etc.) to examine inner structures that would otherwise remain unavailable or require destructive procedures.

### 2.1.1 Interaction of X-rays with matter

EM radiation interacts with matter in three ways: photoelectric effect, Compton scattering and pair production. Because of the energy range where X-rays fall being too low, only the first two are relevant here [19], with their probability depending on various factors as described in this section.

Both effects entail a loss of energy from the incident to the outgoing radiation, that is, it is *attenuated*. The attenuation of X-rays through an object is described by Beer-Lambert law [20]:

$$I = \int_0^{E_{max}} I_0(E) e^{-\int_{-\infty}^{+\infty} \mu(E,x) dx} dE. \quad (2.1)$$

The intensity ( $I$ ) of the beam is characterized in terms of a tissue linear attenuation coefficient ( $\mu$ ) and decreases exponentially. The value of  $\mu$  depends upon the energy of the incident X-rays. Sometimes, it is simplified for a monochromatic beam and homogeneous material, in which case it becomes

$$I = I_0 e^{-\mu x}. \quad (2.2)$$

#### Photoelectric effect

All the energy of the photon is transferred to an electron in one of the atomic shells (typically inner) in an atom of the sample. This electron is ejected and leaves a vacancy that is

occupied by an electron from an outer layer, which involves the emission of characteristic radiation [21]. The probability of this event depends on the energy ( $E$ ) of the incident X-ray, the effective atomic number ( $Z_{eff}$ ) of the sample, and the material density ( $\rho$ ):

$$P_{pe} \propto \rho \frac{Z_{eff}^3}{E^3}. \quad (2.3)$$

### Compton Scattering

In Compton scattering, the interaction is also photon-electron, with the difference that only a portion of the photon's energy is absorbed. The X-ray photon diverts from its original trajectory as a result of the event, whose probability ( $P_{cs}$ ) only depends on the material density ( $\rho$ ) and the energy ( $E$ ).

$$P_{cs} \propto \frac{\rho}{E}. \quad (2.4)$$

The linear attenuation coefficient is the addition of the contribution of both effects ( $\mu = \mu_{pe} + \mu_{cs}$ ). The attenuation coefficient is often characterized as the mass attenuation coefficient  $\mu_{mass} = \frac{\mu}{\rho}$ .

It has been shown how the photoelectric effect has a stronger dependency on energy than Compton scattering. Therefore, it is the dominating factor for attenuation in the lower energy range while scattering is so for the higher energies [22], as depicted in figure 2.1 specifically for soft tissue.

#### 2.1.2 Complex index of refraction

Since X-rays are a form of EM, not only their photon model but also their wave model and its phenomena should be considered. As such, some refraction is expected to happen when the wave encounters a change in the medium of propagation [17].

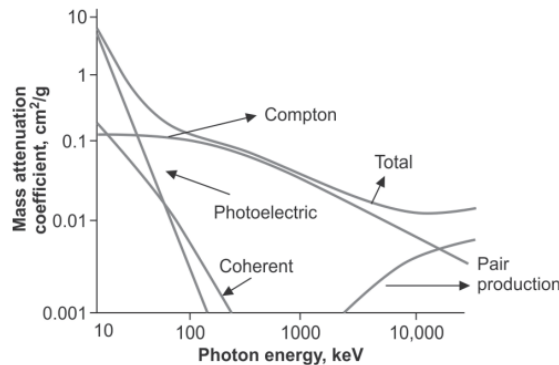


Fig. 2.1. Soft tissue mass attenuation coefficient as function of energy [23].

The complex refractive index for X-rays is usually given as

$$n = 1 - \delta + i\beta, \quad (2.5)$$

where the imaginary part ( $\beta$ ) holds a relationship of proportionality with the linear attenuation coefficient ( $\mu$ ) and is usually much smaller than and the real part ( $\delta$ ), known as the refractive index decrement.

With these two definitions, the propagation of a wave with wave number  $k = \frac{2\pi}{\lambda}$  and amplitude  $A$  along the  $z$  direction in vacuum can be expressed as:

$$\psi_v(z, t) = Ae^{i(kz - \omega t)}. \quad (2.6)$$

In a medium  $n$ , the propagation becomes

$$\psi_n(z, t) = Ae^{i(nkz - \omega t)} = \psi_v(z, t)e^{i(1-\delta)kz}e^{-\beta kz}. \quad (2.7)$$

It is clear from equation 2.7 that the imaginary part of the refractive index modulates the amplitude and that, in that sense, the transmittance of the wave  $T$  after traveling a distance  $d$ :

$$T(d) = \frac{I_m(z=d)}{I_v(z=0)} = \frac{|\psi_m(z=d, t)|^2}{|\psi_v(z=0, t)|^2} = e^{-2\beta kz} \quad (2.8)$$

This expression allows to directly relate the attenuation coefficient to  $\beta$  through the simplified form of Beer-Lambert Law in equation 2.2 as

$$\mu = 2k\beta. \quad (2.9)$$

On the other hand the refractive index decrement is defined as

$$\delta = \frac{r_0 h^2 c^2 \rho_e}{2\pi E^2}. \quad (2.10)$$

with  $r_0$  the classic electron radius,  $h$  Planck's constant,  $c$  the speed of light in vacuum,  $\rho_e$  the electron density, and  $E$  the energy of the X-ray. Furthermore, the electron density can be obtained from its mass density  $\rho_{mass}$ , the mass fractions  $w$ , mass atomic numbers  $A$  and real part of their atomic scattering factors in the forward direction  $f_i^1$  of each of the elements  $i$  that compose it [17]:

$$\rho_e = \rho_{mass} \sum w_i \frac{NA}{A_i} f_i^1. \quad (2.11)$$

It should also be mentioned that the phase difference ( $\phi$ ) may be expressed as function of the decrement index ( $\delta$ ) as

$$\phi = k\delta. \quad (2.12)$$

As a result, the following line integrals indicate the cumulative phase shift ( $\Phi$ ) of the X-ray beam after passing through a material of thickness  $z$  [24]:

$$\Phi = \int \phi(\mathbf{r}) dz. \quad (2.13)$$

Both the discussed effects of absorption and and refraction as explained by the complex index of refraction can be visualized in figure 2.2.

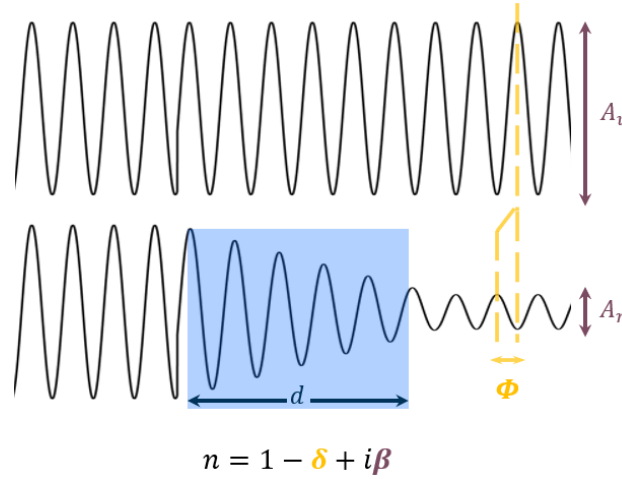


Fig. 2.2. X-ray absorption (red) and phase shift (green) after a change of medium. Inspired by course material from MNT course.

## 2.2 Grating interferometry

The early uses of X-rays were for medical imaging of bones because of their elevated absorption. It was only relatively recently discovered that their phase shift may also be used to generate signals after which Bonse and Hart proposed the first X-ray phase-contrast method in 1965 [25]. It was the later discovery of X-ray propagation PC in 1995 [26] that fueled the interest in this type of imaging [27].

Among the existing PC techniques (crystal interferometry, diffraction enhanced imaging, free-space propagation, etc.), GI [28, 29] is conspicuous because of its capability to separately reconstruct for absorption, PC and small angle scattering. It is a differential PC method, which implies it records the derivative of the phase of the wavefront. Another strength of GI is that upon the addition of a third grating (G0) before the sample, it can be adapted for low coherence and brilliance sources, that is, for traditional X-ray tubes, as was shown in [29].

### 2.2.1 Hardware and working principles

Figure 2.3 depicts the principle of a grating interferometer. The approach is based on detecting fringe positions and determining the form of the wave front from them. The first

grating functions as a beam splitter, creating a phase shift that causes interference fringes at particular distances behind G1 due to the Talbot effect. Local fringe displacement is caused by perturbations of the incident wave front, such as those caused by refraction on a beam object. Because the pitch of G1 falls in the micrometer scale, detectors cannot directly discern fringe location because of their bigger pixel sizes.

An analyzer grating (G2) is employed as a consequence. It works translating local fringe location into signal intensity fluctuation, and should have the direction and pitch of the fringe pattern [28].

The so-called Talbot interferometer only generates meaningful images if the source is temporally and spatially coherent. This can be achieved under a few circumstances: with synchrotron sources (inapplicable to the clinic), with micro-focus X-ray tubes (low power), or liquid-metal jet source (expensive). Therefore, the technique is not easily transferable to a clinical set-up. This issue is tackled by the introduction of a third grating (G0) at the source. The configuration is known as a Talbot-Lau interferometer and it generates a series of individual sources that become coherent at the position of G1 [31].

After an acquisition with said geometry, it is necessary to separate the differential phase signal from that of absorption and small angle scattering. The system employs phase-stepping for this goal. One of the gratings is displaced over one period in the direction  $y_g$  as depicted in figure 2.3. An image is saved for each of the steps of this movement. The intensity signal oscillates as a function of the position of the displacing grating for each pixel (see figure 2.4) [24]. In order to be able to retrieve the signals, it is necessary to use a reference measurement, typically referred to as a *flat scan* that tells about the shape of the wavefront without the distortions introduced by the phase object.

The phase shift in the intensity oscillations ( $\varphi$ ) can be easily related to the differential wavefront phase profile ( $\Phi$ ) if the wavelength ( $\lambda$ ), distance between G1 and G2 ( $d$ ) and the pitch of G2 ( $g_2$ ) are known [29]:

$$\frac{\partial \Phi}{\partial y} = \frac{g_2 \varphi}{d \lambda}. \quad (2.14)$$

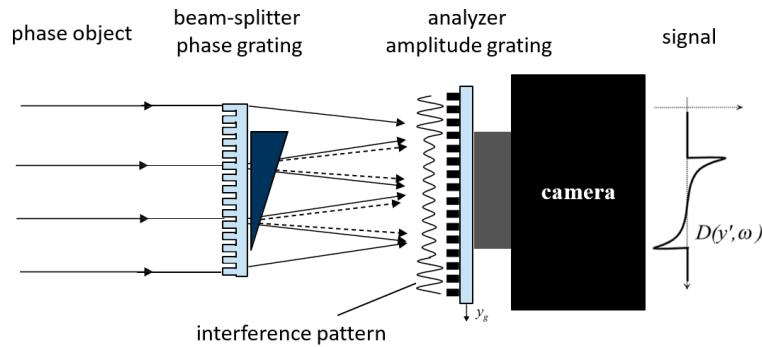


Fig. 2.3. X-ray grating interferometer. Through the arrangement established by the gratings G1 and G2, a phase object in the beam path induces a tiny deflection of x rays, modifying the locally transmitted intensity. Figure using material from [30] and MNT course material.

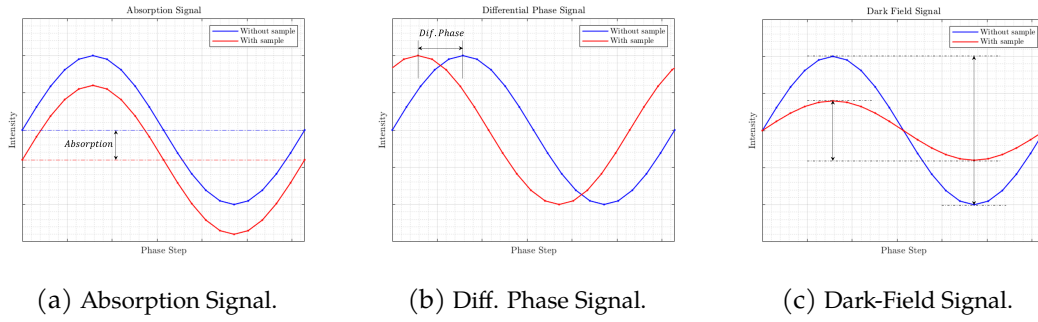


Fig. 2.4. Signal Retrieval in Talbot-Lau Interferometer. The three signals that can be differentiated on a per pixel basis thanks to phase-stepping are (a) absorption contrast, (b) differential phase contrast and (c) dark field or small angle scattering signal.

## 2.3 X-ray tomography

The goal of this section is to explain how the volume distributions of the refractive decrement ( $\delta$ ) and the absorption coefficient ( $\mu$ ) can be retrieved from the absorption and differential phase signals from GI.

### 2.3.1 Computed Tomography

CT is a method for 3D reconstruction of the structure of the sample from a series of images taken at various angles, assuming that these projections correspond to the line integral of a physical quantity across a set of parallel planes [32]. For the mathematical description of CT, the object will be simplified to 2D ( $f(x, y)$ ) and only parallel ray reconstruction will be covered. With the geometry and notation from figure 2.5, the set of all line integral or projection for all angles ( $P(\theta, \ell)$ ) is known as the Radon Transform ( $\mathcal{R}\{f(x, y)\}$ , see equation 2.15) [33]. It can be represented by a sinogram, that uses  $\theta$  and  $\ell$  as coordinates.

$$\mathcal{R}\{f(x, y)\} = P(\theta, \ell) = \int_{-\infty}^{\infty} \int_{-\infty}^{\infty} f(x, y) \delta(x \cos \theta + y \sin \theta - \ell) dx dy, \quad (2.15)$$

where  $\ell$  is a line through the object at a given angle ( $\theta$ ) and  $\delta$  the Dirac delta function.

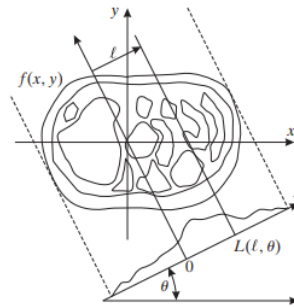


Fig. 2.5. The geometry of lines and projections [32].

$$\ell = x \cos \theta + y \sin \theta. \quad (2.16)$$

Now, moving into the Fourier domain:

$$\begin{aligned} \mathcal{F}\{P(\theta, \ell)\} &= \tilde{P}(\theta, \nu) = \int_{-\infty}^{+\infty} P(\theta, \ell) e^{-2\pi i \nu \ell} d\ell = \\ &= \int_{-\infty}^{+\infty} \int_{-\infty}^{+\infty} f(x, y) e^{-2\pi i \nu [x \cos \theta + y \sin \theta]} dx dy = \\ &= \tilde{f}(\nu \cos \theta, \nu \sin \theta) = \\ &= \mathcal{F}\{f(x, y)\}. \end{aligned} \quad (2.17)$$

The relationship between the 2D Fourier transform (FT) of the scanned object ( $\tilde{f}(\omega \cos \theta, \omega \sin \theta)$ ) and the 1D FT of its projection at a given angle ( $\tilde{P}(\theta, \omega)$ ) exemplified in equation 2.17 is known as the *Fourier Slice Theorem*. It shows that the FT of the projection is a slice of the FT of the object at the same angle that the projection was acquired [32].

### Filtered Back-projection

Filtered back-projection (FBP) is the most common method for tomographic reconstruction. It can be derived from equation 2.17 by applying the inverse Fourier transform (IFT):

$$\begin{aligned} f(x, y) &= \mathcal{F}^{-1}\{\tilde{f}(u, v)\} = \int_{-\infty}^{+\infty} \int_{-\infty}^{+\infty} \tilde{f}(u, v) e^{2\pi i [ux + vy]} du dv = \\ &= \int_0^{2\pi} \int_0^{+\infty} \tilde{f}(\nu \cos \theta, \nu \sin \theta) e^{i\nu [x \cos \theta + y \sin \theta]} \nu d\nu d\theta = \\ &= \int_0^{2\pi} \int_{-\infty}^{+\infty} \tilde{P}(\theta, \nu) \nu e^{i\nu \ell} d\nu d\theta = \\ &= \int_0^{\pi} \int_{-\infty}^{+\infty} \tilde{P}(\theta, \nu) |\nu| e^{i\nu \ell} d\nu d\theta. \end{aligned} \quad (2.18)$$

The term  $|\nu|$  in equation 2.18 gives the name to this method. It corresponds to the so-called *ramp filter* and assigns higher weight to the higher frequencies, which have a lower sampling density. If not accounted for, this would be translated in a loss of fine detail, as is seen in simple back projection. Additionally, it should be pointed out that at least  $N_{\theta, \min} = N_{pixels} \frac{\pi}{2}$  for a reconstruction with good quality.

### 2.3.2 Reconstruction in grating interferometry

Having set the basis of tomographic reconstruction, the next step is to apply it to the signals retrieved from GI, both for absorption and PC.

### Absorption reconstruction

As established in section 2.2.1 and visualized in figure 2.4, the absorption signal is obtained from the average value of the intensity oscillations. The incoming intensity before and after the interaction with the sample  $(I_0, I)$  corresponds to the mean value of the oscillations from the scans without and with the sample in the beam propagation trajectory respectively. From this, according to Beer-Lambert law (equation 2.2) the attenuation coefficient  $(\mu)$  can be related to the signal:

$$\log \frac{\bar{I}_{object}(steps)}{\bar{I}_{flat}(steps)} = \log \frac{I_0}{I} = \int \mu(x', y'; E) dx' \quad (2.19)$$

These quantities can be linked to what was covered so far to apply FBP to it:

$$f(x, y) = \mu(x, y; E), \quad P_\theta(\ell) = \log \frac{I_0}{I} \quad (2.20)$$

Hence, the distribution of attenuation coefficients  $(\mu(x, y))$  can be effectively recovered.

### Phase reconstruction

The reconstruction of the refractive decrement distribution  $(\delta(x, y))$  is more complex because of the differential nature of the signal that is obtained from GI. Combining equations 2.13 and 2.14, the recovered signal  $(\varphi)$  can be linked to the differential phase shift in the wavefront  $(\frac{\partial \Phi}{\partial y'})$  as:

$$\begin{aligned} \varphi &= \frac{\lambda d}{g_2} \frac{\partial \Phi}{\partial y'} = \\ &= \frac{\lambda d}{g_2} \frac{\partial}{\partial y'} \int \phi(x', y') dx' = \\ &= \frac{2\pi d}{g_2} \frac{\partial}{\partial y'} \int \delta(x', y') dx'. \end{aligned} \quad (2.21)$$

where  $d$  is the distance between the G1 and G2 and  $g_2$  is the pitch of G2. The visual representation is given in figure 2.6. The goal for reconstruction is to find the relationship between  $\phi$  and  $\frac{\partial \phi}{\partial y'}$ . In order to establish such relationship, let's make the following associations to use the notation from F. Pfeiffer et al., where  $\omega$  and  $y'$  substitute  $\theta$  and  $\ell$  [30]:

$$G(y', w) = \int \phi(x', y') dx', \quad D(y', w) = \int \frac{\partial \phi(x', y')}{\partial y'} dx'. \quad (2.22)$$

Therefore, the interest is to find the link between the Radon Transform of the projections  $G(y', w)$  and the signal  $D(y', w)$ . Let's start by moving to the Fourier domain:

$$\begin{aligned}
\mathcal{F}\{D(y', w)\} &= \tilde{D}(\nu, \omega) = \int_{-\infty}^{+\infty} \int_{-\infty}^{+\infty} \frac{\partial \phi(x', y')}{\partial y'} e^{-2\pi i \nu y'} = \\
&= \int_{-\infty}^{+\infty} ([\phi(x', y') e^{-2\pi i \nu y'}]_{-\infty}^{+\infty} + 2\pi i \nu \int_{-\infty}^{+\infty} \phi(x', y') e^{-2\pi i \nu y'} dx') = \\
&= 2\pi i \nu \int_{-\infty}^{+\infty} \int_{-\infty}^{+\infty} \phi(x', y') dx' e^{-2\pi i \nu y'} dy' = \\
&= 2\pi i \nu \tilde{D}(\nu, \omega) = \\
&= \mathcal{F}\{G(y', w)\}.
\end{aligned} \tag{2.23}$$

After reaching this point, the phase shift  $\phi(x, y)$  can be recovered using the IFT and the Fourier Slice Theorem as:

$$\begin{aligned}
\phi(x, y) &= \mathcal{F}^{-1}\{\phi(u, v)\} \int_{-\infty}^{+\infty} \int_{-\infty}^{+\infty} \tilde{\phi}(u, v) e^{2\pi i (ux+vy)\nu} dx dy = \\
&= \int_0^{2\pi} \int_{-\infty}^{+\infty} \tilde{\phi}(\nu \cos \omega, \nu \sin \omega) \nu e^{2\pi i \nu (x \cos \omega + y \sin \omega)} d\nu d\omega = \\
&= \int_0^{2\pi} \int_{-\infty}^{+\infty} \tilde{G}(\nu, \omega) \nu e^{2\pi i \nu y'} d\nu d\omega = \\
&= \int_0^{\pi} \int_0^{+\infty} \tilde{G}(\nu, \omega) |\nu| e^{2\pi i \nu y'} d\nu d\omega.
\end{aligned} \tag{2.24}$$

If the relationship from equation 2.23 is applied on the final line from equation 2.24:

$$\begin{aligned}
\phi(x, y) &= \int_0^{\pi} \int_0^{+\infty} \tilde{G}(\nu, \omega) |\nu| e^{2\pi i \nu y'} d\nu d\omega = \\
&= \int_0^{\pi} \int_0^{+\infty} \tilde{D}(\nu, \omega) \frac{|\nu|}{2\pi i \nu} e^{2\pi i \nu y'} d\nu d\omega = \\
&= \int_0^{\pi} \int_0^{+\infty} \tilde{D}(\nu, \omega) \tilde{h}(\nu) e^{2\pi i \nu y'} d\nu d\omega.
\end{aligned} \tag{2.25}$$

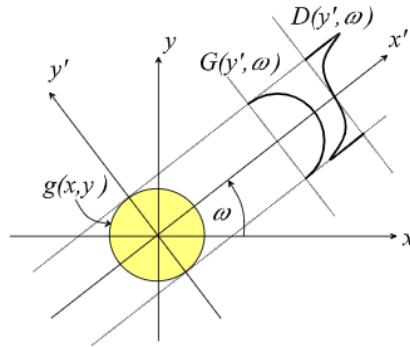


Fig. 2.6. Projection geometry for phase signal [30].

The result from equation 2.25 is similar to FBP except in this case the filter is given by  $\tilde{h}(\nu)$ , which corresponds to the Hilbert filter in the space domain. From equation 2.21, the refractive decrement distribution ( $\delta(x, y)$ ) can be directly calculated from the wavefront phase shift ( $\phi(x, y)$ ).

### 2.3.3 Artifacts in tomography

Most medical imaging technologies produce characteristics that do not reflect a true item within the sample. Artifacts are non-essential traits that may either conceal key aspects or be misinterpreted as anomalous results. The most important in tomographic imaging are [34]:

- **Beam hardening.** It only affects absorption imaging, and arises from the significant beam attenuation caused by certain materials and as a consequence of the attenuation dependency on the energy since the X-ray beam is effectively polychromatic. It shows as broad dark bands or streaks [32].
- **Ring artifact.** It is the most common artifact in CT. A circular artifact will appear if one of the detectors on a third-generation (spinning x-ray tube and detector assembly) scanner is out of calibration [35]. In the sinograms, they show as line artifacts, that tell the element that should have acquired that row/column was faulty.
- **Center of rotation artifact.** Tomographic reconstructions often assume that its location of the center of rotation is known, however this is not always the case. If the presumed center of rotation is wrong, the reconstruction will show half-moon artifacts and stripes, which follow different directions depending on whether the used center of rotation is higher or lower than the real one. The error is different in each slice so it should be corrected for separately [36].
- **Angular undersampling.** One of the defining elements in CT quality is the number of projections employed for reconstruction. Angular undersampling leads to view aliasing, in which stripes radiate at a distance from the border of a dense object [37].

## 2.4 Material decomposition

In medicine, lipid, protein, and water content is an important indication of sickness progression. Tumors have a two-fold greater water content than normal tissue, but have 45 % lower lipid content [38,39]. Collagen content, a crucial structural protein, increases in breast tissues [40,41]. Hepatic steatosis is the abnormal accumulation of lipids in the liver (may reach over 5 % fat in mass) [42]. As is the initial sign and symptom of nonalcoholic liver disease, which affects 20–30 % of the adult population [43], it is of interest for early diagnosis.

The differentiation of the lipid, protein, and water content has traditionally been assessed through different histopathology slide staining and analysis methods [44]. Despite functional, it is not an ideal technique, since it is invasive. CT-based methods would therefore be more suited, but absorption imaging is of limited applicability in soft tissue imaging. Only for tissues containing lipid is it possible to quantify the amounts of the other two components because of the low contrast that is otherwise achieved.

Discrimination between materials is of key importance for a variety of fields, not just clinically. This process, known as *material decomposition* is one of the applications of CT because of quantitative nature and the direct connection between the attenuation coefficient and the mass density. This section will go through the approaches that use only absorption and proceed with the novel use of PC for material decomposition.

### 2.4.1 Using dual energy absorption imaging

Many methods have been presented thus far working on either the pre- [45–47], or the post-reconstruction [48–52] regime. Most of these methods make use of dual energy or spectral CT, which is a CT technology that employs two distinct X-ray spectra to probe materials with varying attenuation qualities at various energies [19].

The methods are based on the idea that the mass attenuation of a material ( $\mu_m$ ) with two or more components can be expressed as the weighted average of the coefficients of its  $N$  individual basis materials ( $\mu_{m,i}$ ), that is:

$$\mu_m(E) = \sum_{i=1}^N w_i \mu_{m,i}(E), \quad (2.26)$$

where  $w_i$  are the corresponding mass fraction of each of the constituent parts (what is to be found). For spectral CT, two different energies are used, which means that the decomposition would be effective for only two basis materials. Assuming that  $\sum_i^N w_i = 1$  allows expansion to three materials [51].

### 2.4.2 Using phase and absorption imaging

Given the recent development of PC X-ray imaging techniques, the same approach can be used substituting the attenuation coefficient from a second energy for the refractive decrement that they retrieve.

This can be advantageous when dealing with biological samples that yield poor contrast in absorption imaging, which hinders the separability in material decomposition. The complementary information provided by the PC images was explored by Willner et al in [15] for protein, lipid and water as basis materials.

# Materials

This section briefly discloses the resources that have been used for the development of the project, detailing the imaging setup, sample properties and the software tools employed to tackle the decomposition problem.

## 3.1 Static set-up

The GI geometry is displayed in figure 3.1. The X-ray source corresponds to the model MXR-225HP/11 manufactured by Comet Holding AG, operated at 70 kVp and 200 mA. The detector matches a DECTRIS® prototype with a 750  $\mu\text{m}$  thick CdTe sensor, a pixel size of 75  $\mu\text{m}$  and a size of  $256 \times 3072$  px. In terms of the geometry, the distance between the source and the center of rotation ( $a$ ) is of 1030 mm, and that between the rotation center and the detector ( $b$ ) of 740 mm. It is a 4.2  $\mu\text{m}$ -pitch symmetric setup with G1 for a  $\pi$ -shift at 46 keV.

## 3.2 Phantom properties

Two polymethyl methacrylate (PMMA) phantoms with the same design were used for this project. They are cylindrical and have cylindrical cavities that were filled with different materials, as follows:

- **Phantom 1.** Acetone, canola oil, distilled water, ethanol and glycerol.

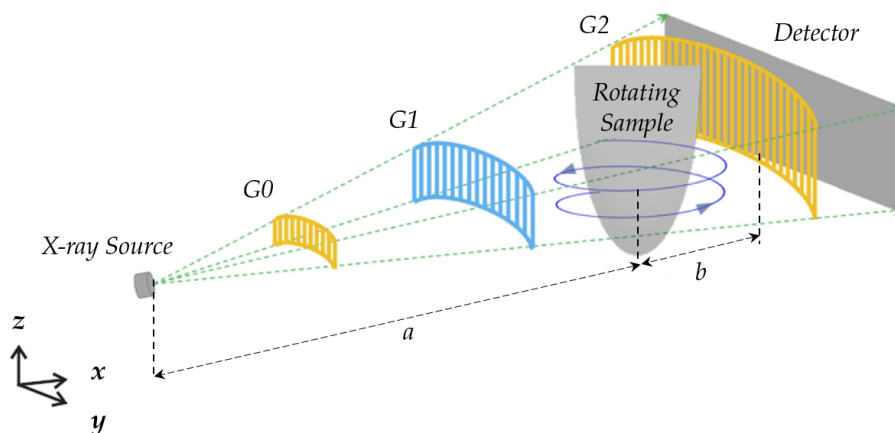


Fig. 3.1. GI geometry. Figure from [53].

- **Phantom 2.** Canola oil, distilled water, ethanol and polyoxymethylene (POM).

For reference, the mass fraction element composition of each of these materials is in table 3.1. The average density and composition of canola oil was retrieved from [54].

TABLE 3.1. COMPOSITION OF PHANTOM ELEMENTS

Material	Formula	density [kg/m <sup>3</sup> ]	H	C	O
Acetone	$C_3H_6O$	784	0.104	0.620	0.275
Canola oil	-	915	0.119	0.760	0.121
Ethanol	$C_2H_6O$	789	0.131	0.521	0.347
Glycerol	$C_3H_8O_3$	1260	0.088	0.391	0.521
PMMA	$C_5O_2H_8$	1180	0.081	0.600	0.320
POM	$CH_2O_3$	1410	0.067	0.400	0.533
Water	$H_2O$	1000	0.112	0	0.888

It should be mentioned that the phantoms had radii of 2.5 and 3 cm, with wells of 0.7 cm of radius. Figure 3.2 shows a schematic of the phantoms and images of them as they were scanned.

### 3.3 Meat properties

A small piece of bacon was scanned to evaluate the effectiveness of the decomposition method on an approximation of human tissue. It was vacuumed, submerged in water and attached to the bottom of the PMMA container using double-sided tape and a POM platform, as can be observed in figure 3.3.

For reference, the composition of pure proteins and lipids was taken from [55], while the average protein density was found in [56]. The specifics in table 3.2. The chosen lipid

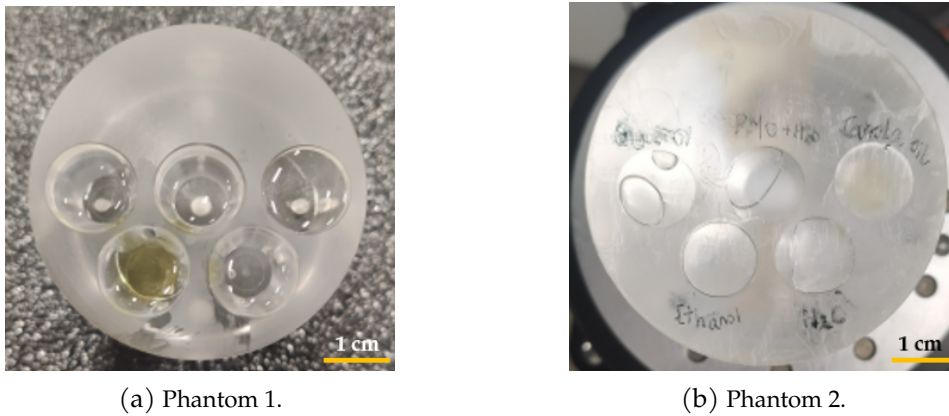


Fig. 3.2. Scanned phantoms. From left to right and top to bottom, phantom 1 in (a) is filled with ethanol, acetone, glycerol, canola oil and water. In the same order, phantom 2 (b) is filled with glycerol, POM, canola oil, ethanol and water.

is glycerol trioleate because it belongs to the family of triglycerides, main components of adipose tissue.

TABLE 3.2. COMPOSITION OF LIPIDS AND PROTEINS

Material	density [ $\frac{kg}{m^3}$ ]	H	C	N	O	S
Protein	1410	0.066	0.534	0.170	0.220	0
Glycerol trioleate	921	0.118	0.774	0	0.108	0.010

### 3.4 Software

This project has been developed in Python™ v3.8 in the 64 bit version. Several steps of the preprocessing made use of the NeuTomPy [57] and TomoPy [58] toolboxes while reconstruction made use of the ASTRA Toolbox [59].



(a) Profile view.



(b) Top view.

Fig. 3.3. Scanned bacon piece. Top was covered with plastic wrap to prevent splashes.

# Methods

---

This section presents all the steps followed for the development of the project. All the data that is mentioned was acquired with the static setup of the GI in the lab at PSI. The data served two tasks: (1) assessing the precision of the system in retrieving the attenuation coefficient and refractive decrement values and (2) implementing material decomposition.

## 4.1 Sample preparation and scanning

This is intended as an outline of how the tomographic acquisitions were performed, stating all the steps of acquisition and pre-processing until the extraction of the reconstructed volume. It is worth mentioning that a vertical scan was performed as a first step to select the part of the sample that will be scanned. Additionally the alignment of the gratings was also checked beforehand. The rest of the steps were as follows:

- 1) **Acquisition details.** It used a cone beam geometry for both the flat-field and the tomographic measurements. One scan was performed on phantom 1, while there were 11 for phantom 2 and the bacon sample.
  - i) *Flat-field measurements* were taken before and after every scan to account for any instabilities arising while the sample is imaged. The acquisition lasts 10 s.
  - ii) *Phase steps:* 5 with one full rotation of the sample per step.
  - iii) *Number of frames.* With a frame rate of 10 and 20 frames/s for the first and second phantom respectively, taking 1 min to do the rotation, there were 600 and 1200 frames/step.
- 2) **Signal retrieval**
  - i) *Binning.* The amount of pixels was reduced by four by averaging the intensity values of 4 pixels.
  - ii) *Flat-field averaging.* All the frames in each flat scan are averaged.
  - iii) *Signal retrieval.* The real period of the intensity sinusoidal that is recorded per pixel along steps is obtained using the flat-field data. With it, the phase ( $\alpha$ ), intensity ( $I$ ) and visibility ( $v$ ) signals are obtained using least squares to fit  $a\sin x + b\cos x + c$  to the sinusoidal. Given that  $a\sin x + b\cos x + c = \sqrt{a^2 + b^2} \cos(x - \alpha) + c$ :

$$I = c, \quad \alpha = -\tan^{-1}\left(\frac{a}{b}\right), \quad v = \frac{\sqrt{a^2 + b^2}}{c} \quad (4.1)$$

- iv) *Relation to the wavefront.* The previous step yields one sinogram per signal, but it is not related to the wavefront but to a generic sinusoidal that is used as reference. The relation to the wavefront also serves as flat-field correction and allows to retrieve values for the attenuation line integrals, the pattern phase shift ( $\varphi$ ) and line integrals of diffusion:

$$\int \mu dx = \log \frac{I_{flat}}{I}, \quad \varphi = \alpha - \alpha_{flat}, \quad \int \varepsilon dx = \log \frac{v_{flat}}{v}, \quad (4.2)$$

with  $\varepsilon$  the diffusion coefficient. As was covered in equation 2.21, the pattern phase shift can be related to the differential accumulated phase shift in the wavefront as  $\frac{\partial \Phi}{\partial y} = \frac{g_2 \varphi}{\lambda d}$ . Thus, the three sinograms are obtained and effectively related to their physical meaning. It should be noted that the diffusion data will not be mentioned further in this report as it does not pertain the scope of the project.

- 3) **Sinogram processing.** This step reduces the effects of some of the common artifacts in tomographic imaging.
- i) *Beam hardening correction.* Using data from a past measurement of PMMA plates without the gratings, the relationship between the intensity of the beam and the thickness of the plates was found per pixel. The inverse of that relationship was used for correction as is the current approach in the lab.
  - ii) *Center of rotation adjustment.* the center of rotation is found through and the sinogram columns shifted accordingly.
  - iii) *Ring artifact removal.* Found to be one of the most notorious problems, it was addressed with the NeuTomPy toolbox before reconstruction, which works in the Fourier-Wavelet space, while after the reconstruction a method from the TomoPy toolbox was employed.
- 4) **Reconstruction** uses the ASTRA Toolbox, which requires to specify the geometry (cone-beam), and the method to be employed for each reconstruction: FBP for the attenuation sinograms and simple back-projection to the phase-shift sinogram after the Hilbert filter has been applied projection-wise (each sinogram row). The reconstruction therefore yields the linear attenuation and refractive index decrement distributions  $\mu(x, y)$  and  $\delta(x, y)$ .

Before further discussion, it should be mentioned that despite interest in generating a continuous phase map, it was not possible to perfectly align the three G2 gratings. That created discontinuities (see figure 4.1) that impacted the quality of the reconstruction as an artifact source.

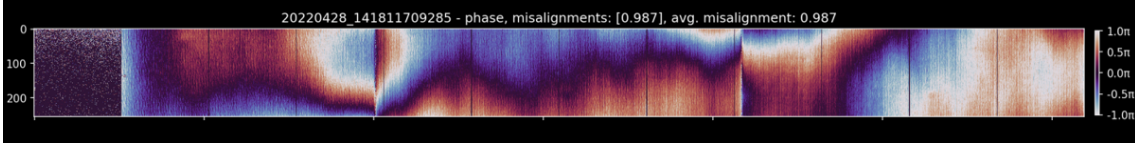


Fig. 4.1. Flat field phase map of the grating interferometer.

## 4.2 System assessment

Once the reconstructed volumes were available, the the precision of the system in retrieving the linear attenuation coefficient ( $\mu(x, y)$ ) and refractive index decrement ( $\delta(x, y)$ ) was evaluated. The idea was to compare the values of the reconstructed to the theoretical values of each of the materials in the phantoms. This involved several steps, disclosed henceforth.

### 4.2.1 Calculation of retrieved values

The procedure to obtain the  $\mu$  and  $\delta$  for each material consisted in calculating the mean and standard deviation ( $\bar{x} \pm \Delta x$ ) of each material region. Before averaging, both reconstructions were smoothed using 3D anisotropic diffusion. The choice of this filter was based on the fact that it performs no smoothing across edges unlike gaussian smoothing, which allowed for it to be used in the slice plane. It did not homogenize the influence of ring artifacts, which was sought after. Succeeding to smoothing, the vertical profile of each material was analyzed to determine which range of slices was to be averaged (top and bottom did not contain the filling materials).

### 4.2.2 Calculation of effective energies and theoretical values

Both  $\mu$  and  $\delta$  are dependent on the energy of the beam spectrum. That means that a value needs to be found to be used as reference when the theoretical values for each material are calculated. With this in mind, the mean values  $\bar{\mu}$  and  $\bar{\delta}$  for PMMA were selected to calculate the effective energy for each material, separately for the  $\mu$  and  $\delta$  reconstructions.

#### Effective energies

In the case of the attenuation coefficient, the element mass attenuation coefficients from the National Institute of Standards and Technology (NIST) database [60] were used along with the material composition as listed in table 3.1 through

$$\mu_L = \rho_m \sum_{i=0}^N w_i \mu_{m,i}, \quad (4.3)$$

where the linear attenuation coefficient ( $\mu_L$ ) comprised of  $N$  elements is found by the weighted average of the mass attenuation of each of the elements ( $\mu_{m,i}$ ) using their mass

fractions ( $w_i$ ) and the mass density of the material ( $\rho_m$ ).

The theoretical  $\mu_L$  for the energy range of 30 – 100 keV was obtained, followed by interpolation of  $\bar{\mu}$  to retrieve the corresponding energy value, taken as effective energy for attenuation ( $E_\mu$ ).

The procedure to get the effective energy for refractive decrements ( $E_\delta$ ) was identical. It used equations 2.10 and 2.11 with table 3.1 and  $f_1$  values from the database for X-ray applications (DABAX) [61, 62] to calculate the theoretical  $\delta$  values in the same energy range, followed by interpolation of  $\bar{\delta}$  to determine  $E_\delta$ .

### Theoretical values

With  $E_\mu$  and  $E_\delta$  it was possible to retrieve the theoretical values of the attenuation coefficients ( $\mu_t$ ) and the refractive index decrements ( $\delta_t$ ) via interpolation, again with the NIST and DABAX tables respectively.

#### 4.2.3 Measurement of precision

Having  $\mu_t$ ,  $\delta_t$ ,  $\bar{\mu}$  and  $\bar{\delta}$ , the precision of the system was evaluated using the relative uncertainty of each  $\bar{\mu}_i$  and  $\bar{\delta}_i$  as well as the relative error with respect to  $\mu_{t,i}$  and  $\delta_{t,i}$

$$Uncertainty[\%] = 100 \times \frac{\Delta x}{\bar{x}}. \quad (4.4)$$

$$Error[\%] = 100 \times \frac{|x_t - \bar{x}|}{x_t}. \quad (4.5)$$

### 4.3 Material decomposition

The idea behind material decomposition for attenuation was overviewed in section 2.4.1. Equation 2.26 can be expressed in terms of the linear attenuation coefficients ( $\mu_l$ ) as

$$\begin{aligned} \mu_l &= \rho_m \mu_m = \rho_m \sum_{i=0}^N w_i \mu_{m,i} = \\ &= \rho_m \sum_{i=0}^N w_i \frac{\mu_{l,i}}{\rho_{m,i}} = \\ &= \rho_m \sum_{i=0}^N \frac{m_i}{\sum_{j=0}^N m_j} \frac{\mu_{l,i}}{V_i} = \\ &= \frac{\sum_{j=0}^N m_j}{\sum_{j=0}^N V_j} \sum_{i=0}^N \mu_{l,i} \frac{V_i}{\sum_{j=0}^N m_j} = \\ &= \sum_{i=0}^N \frac{V_i}{\sum_{j=0}^N V_j} \mu_{l,i} = \sum_{i=0}^N \gamma_i \mu_{l,i}. \end{aligned} \quad (4.6)$$

The expression assumes the object is an ideal mixture (such that volume conservation applies), where  $\gamma_i$  is the volume fraction of each basis material. A similar expression may be found for  $\delta$  following the same rationale:

$$\delta = \sum_{i=0}^N \gamma_i \delta_i. \quad (4.7)$$

To allow for three-material decomposition, an additional constrain is needed. In this case, it is assumed that the tissue is exclusively composed by protein, lipid and water. With  $P$ ,  $L$  and  $W$  the volume fractions of the three components, the system of linear equations can be written in matrix form as:

$$\begin{bmatrix} \mu \\ \delta \\ 1 \end{bmatrix} = \begin{bmatrix} \mu_l & \mu_p & \mu_w \\ \delta_l & \delta_p & \delta_w \\ 1 & 1 & 1 \end{bmatrix} \begin{bmatrix} L \\ P \\ W \end{bmatrix} = A \begin{bmatrix} L \\ P \\ W \end{bmatrix}, \quad (4.8)$$

where  $\mu_l, \mu_p, \mu_w, \delta_l, \delta_p, \delta_w$  are the  $\mu$  and  $\delta$  values for pure protein, lipid and water, which can be calculated for a certain energy using the NIST and DABAX tables together with the mass fractions from table 3.2. As for the phantoms, the effective energy calculation took PMMA as reference. The average values for the thermoplastic were extracted from circular regions in the walls of the container, as were those from a section of the same size for water.

The values of each voxel do not entirely correspond to the physical entity that is reconstructed. Instead, there is an additional contribution from noise and artifacts, denoted here as  $e$ . Hence, equation 4.8 becomes

$$y = A\gamma + e. \quad (4.9)$$

The solution that minimizes the error term can be found through least-squares as:

$$\hat{\gamma} = (A^T A)^{-1} A^T y. \quad (4.10)$$

The ideal implementation of least-squares should be bounded to the range  $[0, 1]$  since the solution is found for volume fractions. The bounded approach from SciPy was not used for timing reasons, being replaced with the non-negative version, which provided sufficient regularization.

# Results and Discussion

---

The results obtained in the methods will be presented and discussed in this section, starting with the evaluation of the system's precision, continuing with the analysis of material decomposition.

## 5.1 Image acquisition

The results from the acquisition and pre-processing parameters as specified in section 4.1 can be visualized in figure 5.1. The images, despite sharp, are not devoid of artifacts: rings are pronounced in all three scans. The fact that they are not smoothed for Phantom 2 and the bacon sample indicates that they are stable (see figures 5.1.b and 5.1.c), given that they are the average of 11 scans. They may originate from an imperfect alignment of the G2 gratings, which would exert a continuous influence on the signal throughout the scanning session. As will be discussed subsequently, the influence of these artifacts on the final results is not minor, since they alter the values of the attenuation and refractive index decrement separating them from their ideal value.

The selection of slices used for the retrieval of the mean values was restricted to 108 slices (8 to 115) as that was the region that maintained a constant value (after smoothing) for all the materials (see figures A.1 and A.2).

## 5.2 System assessment

### 5.2.1 Calculated values

Following the described procedures and taking PMMA as reference, the effective energies are  $E_\mu = 50.61$  and  $E_\delta = 46.68$  keV for Phantom 1 and  $E_\mu = 49.64$  and  $E_\delta = 49.60$  keV for Phantom 2. All the values are higher than the 46 keV the interferometer was designed for as a consequence of the beam hardening after traversing the sample, but it is comparable for all measurements (with a standard deviation  $\sigma = 1.32$ ).

Tables 5.1 and 5.2 contain the results of the retrieval of the mean attenuation coefficients and refractive index decrements with their respective standard deviation and the values at estimated effective energies ( $\bar{x} \pm \Delta x$  and  $x_t$ ).

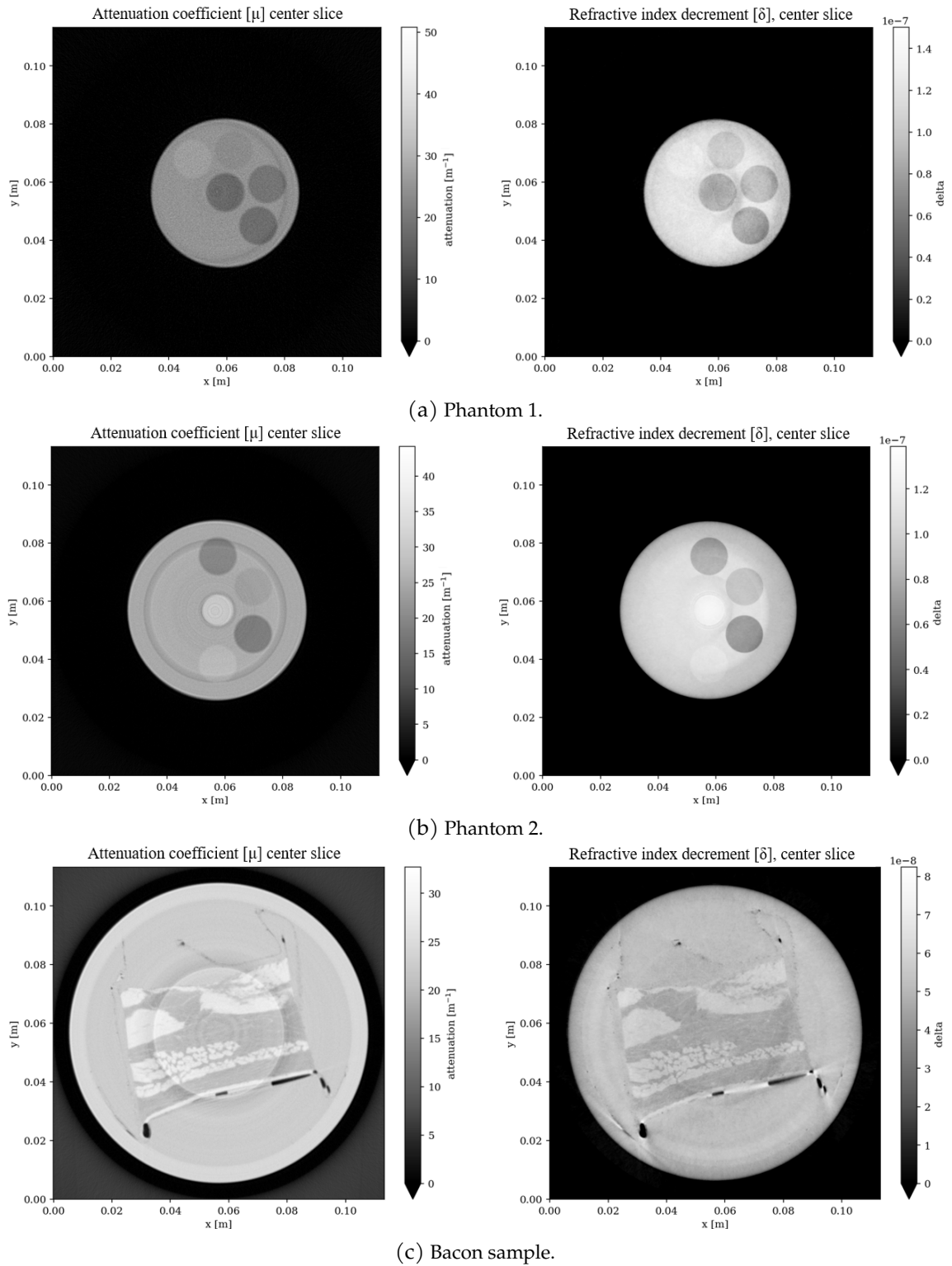


Fig. 5.1. Center slice of acquired volumes. Phantom 1 (a) was only scanned once. The average of 11 scans is shown for Phantom 2 (b) and the bacon sample (c).

### 5.2.2 Analysis of results

Figures A.3 and A.4 offer a clear overview of the results. The histogram of the volumes of both phantoms and for both attenuation and PC after smoothing shows very distinct peaks that can be closely linked to mean values displayed in tables 5.1 and 5.2. A closer look at the individual histograms from each of the considered cylindrical regions qualitatively portrays that the system is indeed precise, since there are only small differences between the effective and mean values of  $\mu$  and  $\delta$ .

Because of the lack of across-edge smoothing, the individual histograms also show the impact of the ring and shadowing artifacts as a secondary normal distribution to the main mean peak. This is especially notorious in the PC volumes, where the shadowing artifacts extend into larger regions. The effect it has over the  $\bar{\delta}$  is manifest in the glycerol and canola oil wells from Phantom 2.

Quantitatively, the precision is shown in the values of percentage relative uncertainty and error from table 5.3. There, it can be observed that both measures are generally lower for Phantom 2, which stems from the better statistics provided by the averaging of the 11 scans that comprised the scanning session. At the same time, the results are inferior for the refractive index decrements compared to attenuation coefficients, partly a result of the shadow artifacts.

Starting with attenuation, uncertainty, which reveals how dispersed the distributions are, is low. It is highest for ethanol in both phantoms. Although the ring is present in both ethanol cylinders does not deviate the  $\bar{\mu}$  from the one expected at  $E_\mu$  given that it still falls close to the peak of the distribution as shown by the histograms, it increases

TABLE 5.1. PHANTOM 1 ATTENUATION AND REFRACTIVE DECREMENT

Material	$\bar{\mu}$	$\Delta\mu$	$\mu_t$	$\bar{\delta}$	$\Delta\delta$	$\delta_t$
Acetone	0.176	0.009	0.168	8.63E-08	4.37E-09	8.25E-08
Canola Oil	0.195	0.007	0.194	9.43E-08	6.22E-09	9.75E-08
Ethanol	0.181	0.009	0.174	8.32E-08	7.41E-09	8.50E-08
Glycerol	0.265	0.004	0.275	1.27E-07	3.42E-09	1.31E-07
PMMA	0.249	0.004	0.249	1.21E-07	4.48E-09	1.21E-07
Water	0.235	0.004	0.233	1.04E-07	3.76E-09	1.06E-07

TABLE 5.2. PHANTOM 2 ATTENUATION AND REFRACTIVE DECREMENT

Material	$\bar{\mu}$	$\Delta\mu$	$\mu_t$	$\bar{\delta}$	$\Delta\delta$	$\delta_t$
Canola Oil	0.196	0.009	0.195	7.96E-08	5.68E-09	8.64E-08
Ethanol	0.185	0.010	0.175	7.19E-08	5.37E-09	7.53E-08
Glycerol	0.267	0.008	0.278	1.09E-07	5.22E-09	1.16E-07
POM	0.297	0.004	0.301	1.26E-07	2.72E-09	1.27E-07
PMMA	0.252	0.003	0.251	1.08E-07	2.18E-09	1.08E-07
Water	0.236	0.004	0.236	9.17E-08	2.80E-09	9.39E-08

TABLE 5.3. PHANTOM RELATIVE UNCERTAINTY AND ERRORS

Phantom	Material	Uncertainty $\mu$ [%]	Error $\mu$ [%]	Uncertainty $\delta$ [%]	Error $\delta$ [%]
1	Acetone	5.139	4.862	5.068	4.561
	Canola Oil	3.631	0.816	6.600	3.312
	Ethanol	5.172	4.323	8.910	2.117
	Glycerol	1.673	3.58	2.701	3.075
	PMMA	1.471	-	3.685	-
	Water	1.814	0.782	3.626	1.956
2	Canola Oil	4.707	0.695	7.138	7.823
	Ethanol	5.543	5.733	7.466	4.483
	Glycerol	2.845	3.877	4.797	6.069
	POM	1.286	3.199	2.159	0.724
	PMMA	1.243	-	2.023	-
	Water	1.813	0.200	3.056	2.185

$\Delta\mu$ . The values of the ring and those from ethanol are close, which seemingly integrates the ring into  $\mu$  distribution. The relative error remains below 6 %, being the highest for acetone in Phantom 1 and ethanol in Phantom 2. In the case of acetone, it stems directly from the ring artifact, whereas for ethanol the error is genuine and therefore originates in a combination of an imperfect calibration (on PMMA instead of a simulation) and the system itself.

As for the refractive index decrements, uncertainty oscillates more significantly but remains below 10 % in all cases. It is the most prominent for ethanol in both phantoms, a consequence of the shadowing that in this case differentiates the mean of the distributions from the main peak. The top relative error is found for acetone (Phantom 1) and canola oil (Phantom 2). The shadows play a dominating role in all high errors for  $\bar{\delta}$ , since where not present, the error drops (see water in A.3 and A.4).

Figure 5.2 shows that the system is precise enough to enable material separation despite the described influence exerted by the various artifacts. It also shows the relationship between  $\mu$  and  $\delta$  is approaching linearity, as is expected in the energy range of the scan, where Compton scattering begins to dominate attenuation (figure 2.1). This can be considered a limitation for the performance of material decomposition because as will be explained in the following section, it makes the reference points used for the decomposition fall along the same line.

### 5.3 Material decomposition

The method for material decomposition was successfully applied on the attenuation and PC reconstructions of the bacon sample scan (figure 5.3). The least-squares method chosen to solve the pixel-wise problem was the *non-negative* implementation from SciPy instead of the the bounded solution to the range  $[0, 1]$  because of time reasons.

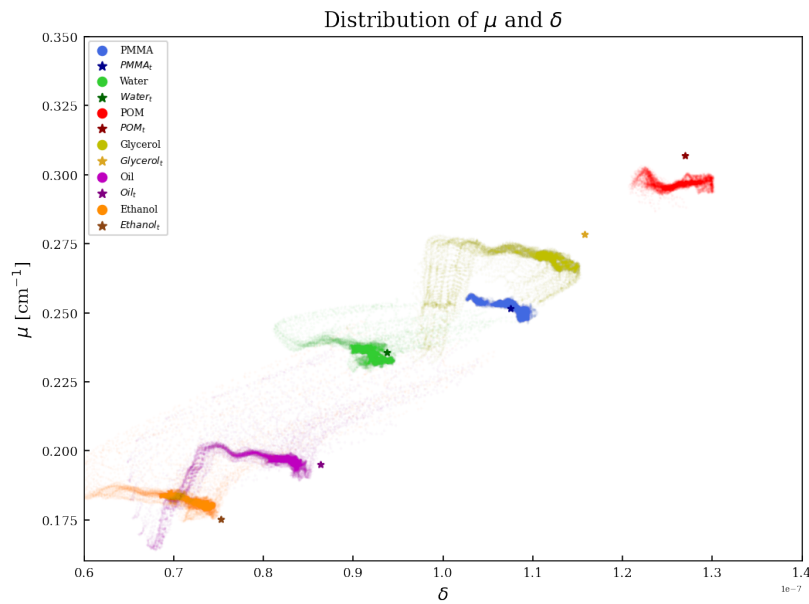
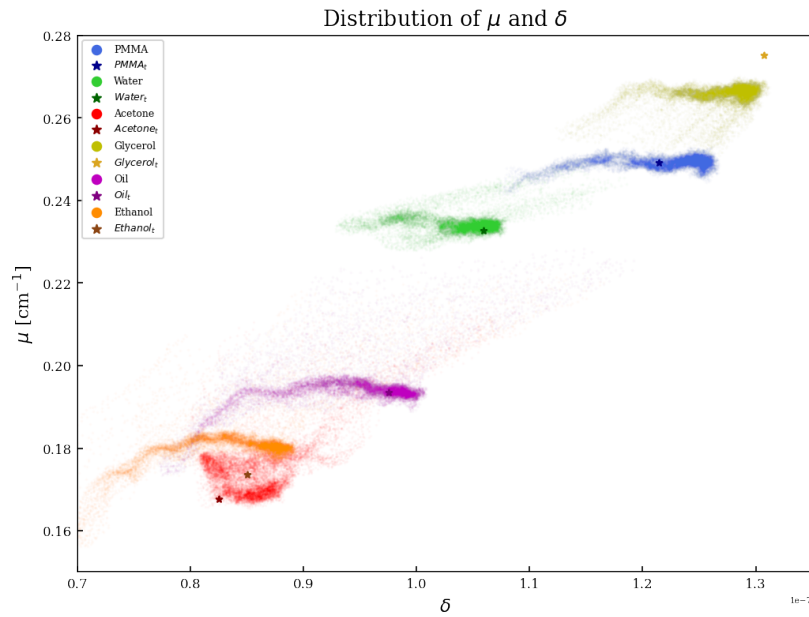


Fig. 5.2. Scatter plot  $\mu$  and  $\delta$  for phantoms 1 (a) and 2 (b) shows that materials are separable based because of the precision of the system.

In order to find the theoretical values for  $\mu$  and  $\delta$  for protein and lipid, the previously discussed method (section 4.2.2) was used. This required the calibration of the effective energy from PMMA. The extraction of  $E_\delta$  was problematic because of the very strong shadowing effects. As a consequence, the edge of the walls of the container are indistinguishable from water as seen in figure 5.3. In fact, it was numerically found to stand at  $E_\delta = 80.78$  keV, which is not feasible given that the beam operates at 70 kVp.

The problem was tackled by manually adjusting  $E_\delta$  to calculate the protein and lipid  $\delta$

values. The chosen energy was 68 keV, as this enabled the basis materials'  $\mu$  and  $\delta$  values to form a triangle that encompasses the data distribution as may be visualized in figure A.5.

Despite the described limitation, the decomposition was achieved. The region that is highlighted as protein corresponds to the lighter regions within the meat attenuation reconstruction, which is congruent with reality: protein is denser than fat, which results in higher attenuation coefficient and thus, lighter pixel values. Same applies to the other two basis materials. The decomposition is especially visually precise inside the inner ring, one of the few regions where water is recognize as water only with no lipid and protein content.

## 5.4 Limitations and future work

The main limitation for the completion of the project originated in the artifacts from the imaging system. The rings that are produced by the slight misalignment of the G2 gratings, which produces a discontinuity in the phase maps that directly impact the values of the reconstruction of the attenuation and PC volumes. As has been stated, this is the main obstacle in the quantitative consideration of the pixel values, which is a must to tackle decomposition analytically with methods such as the one proposed here.

The above accentuates once more the importance of finding reliable  $\mu$  ways to remove

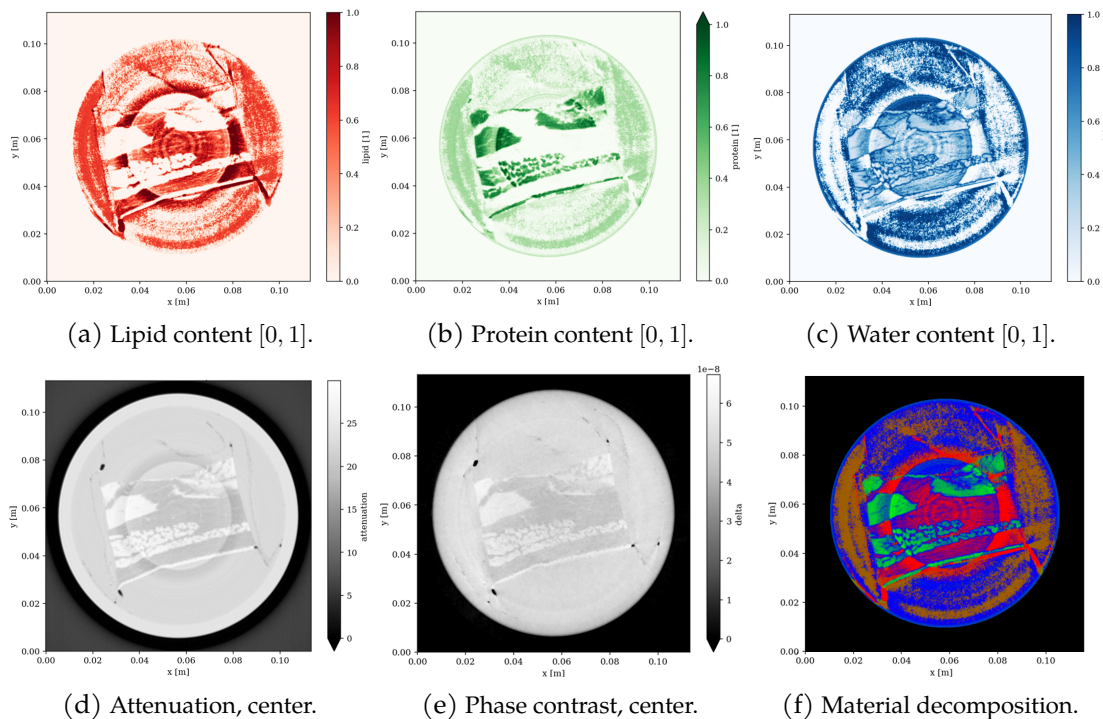


Fig. 5.3. Material decomposition applied on the volumes from the bacon sample. The lipid (a), protein (b) and water (c) maps combined make the color-map in (f) as its RGB channels respectively.

the ring artifacts that do not induce blurring or diminish the quantitative precision of the system. Longer exposition times, provided, for instance, by more scans or slower rotation would improve the statistics by averaging the effects of quantum noise that are inherent to X-rays, but as has been shown, the ring and shadowing artifacts would likely prevail.

Therefore, the first step should be addressing this issue. A search of an ideal set of parameters of the pre-processing methods would be appropriate. The alignment of the three G2 gratings could also be optimized to obtain a continuous phase map. Next should come the development or implementation of more complex methods that target ring artifacts.

In terms of material decomposition, the pipeline to follow would be to use the method on real mammography images. The decomposition could also be implemented for a different trio of basis materials, such as by substituting protein or water for glandular tissue. Once the method has been proven to work on the target data, it will be included in the pipeline for reconstruction and analysis.

# Conclusions

---

The assessment of the system was a confirmation of the quantitative capability of the imaging geometry, acquisition, and pre-processing pipeline that is used in the static-setup. The main outcomes of this project may be summarized as follows:

- The imaging system is quantitative. It is able to retrieve the attenuation coefficient and refractive index decrement distributions in the scanned samples accurately. The highest relative error with respect to the calculated theoretical values stood below 6 and 8 % respectively.
- The relationship between attenuation and refraction is close to linear for a source operating at an effective energy of  $E_{eff} = 46$  keV before the sample, which results in a narrowing of the decomposition space.
- Material decomposition is successful despite the artifacts and the reduced separation space.
- Artifacts are one of the main contributors to such relative error. They can significantly deviate a pixel value from its ideal.

# Bibliography

- [1] H. Sung, J. Ferlay, R. L. Siegel, M. Laversanne, I. Soerjomataram, A. Jemal, and F. Bray, "Global cancer statistics 2020: GLOBOCAN estimates of incidence and mortality worldwide for 36 cancers in 185 countries," *CA Cancer J. Clin.*, vol. 71, no. 3, pp. 209–249, May 2021.
- [2] EU, "European cancer information system," 2022, accessed: 2010-09-30. [Online]. Available: <https://ecis.jrc.ec.europa.eu>
- [3] S. W. Duffy, L. Tabár, A. Yen, Ming-Fang, P. B. Dean, R. A. Smith, H. Jonsson, S. Törnberg, S. L.-S. Chen, S. Y.-H. Chiu, J. C.-Y. Fann, M. M.-S. Ku, W. Y.-Y. Wu, C.-Y. Hsu, Y.-C. Chen, G. Svane, E. Azavedo, H. Grundström, P. Sundén, K. Leifland, E. Frodis, J. Ramos, B. Epstein, A. Åkerlund, A. Sundbom, P. Bordás, H. Wallin, L. Starck, A. Björkgren, S. Carlson, I. Fredriksson, J. Ahlgren, D. Öhman, L. Holmberg, and T. H.-H. Chen, "Mammography screening reduces rates of advanced and fatal breast cancers: Results in 549,091 women," *Cancer*, vol. 126, no. 13, pp. 2971–2979, Jul. 2020.
- [4] J. Brodersen and V. D. Siersma, "Long-term psychosocial consequences of false-positive screening mammography," *The Annals of Family Medicine*, vol. 11, no. 2, pp. 106–115, Mar. 2013. [Online]. Available: <https://doi.org/10.1370/afm.1466>
- [5] M. A. Durand, S. M. Friedewald, D. M. Plecha, D. S. Copit, L. D. Barke, S. L. Rose, M. K. Hayes, L. N. Greer, F. M. Dabbous, and E. F. Conant, "False-negative rates of breast cancer screening with and without digital breast tomosynthesis," *Radiology*, vol. 298, no. 2, pp. 296–305, Feb. 2021. [Online]. Available: <https://doi.org/10.1148/radiol.2020202858>
- [6] C. Canelo-Aybar, D. S. Ferreira, M. Ballesteros, M. Posso, N. Montero, I. Solà, Z. Saz-Parkinson, D. Lerda, P. G. Rossi, S. W. Duffy, M. Follmann, A. Gräwingholt, and P. Alonso-Coello, "Benefits and harms of breast cancer mammography screening for women at average risk of breast cancer: A systematic review for the european commission initiative on breast cancer," *Journal of Medical Screening*, vol. 28, no. 4, pp. 389–404, Feb. 2021. [Online]. Available: <https://doi.org/10.1177/0969141321993866>
- [7] S. Iranmakani, T. Mortezaazadeh, F. Sajadian, M. F. Ghaziani, A. Ghafari, D. Khezerloo, and A. E. Musa, "A review of various modalities in breast imaging: technical aspects and clinical outcomes," *Egypt. J. Radiol. Nucl. Med.*, vol. 51, no. 1, Dec. 2020.
- [8] T. M. Kolb, J. Lichy, and J. H. Newhouse, "Comparison of the performance of screening mammography, physical examination, and breast US and evaluation of factors that influence them: an analysis of 27,825 patient evaluations," *Radiology*, vol. 225, no. 1, pp. 165–175, Oct. 2002.

- [9] F. Diekmann and U. Bick, "Breast tomosynthesis," *Seminars in Ultrasound, CT and MRI*, vol. 32, no. 4, pp. 281–287, 2011, breast Cancer Screening and Diagnosis: State of the Art. [Online]. Available: <https://www.sciencedirect.com/science/article/pii/S0887217111000436>
- [10] S. T. Taba, T. E. Gureyev, M. Alakhras, S. Lewis, D. Lockie, and P. C. Brennan, "X-ray phase-contrast technology in breast imaging: Principles, options, and clinical application," *AJR Am. J. Roentgenol.*, vol. 211, no. 1, pp. 133–145, Jul. 2018.
- [11] S. D. Auweter, J. Herzen, M. Willner, S. Grandl, K. Scherer, F. Bamberg, M. F. Reiser, F. Pfeiffer, and K. Hellerhoff, "X-ray phase-contrast imaging of the breast—advances towards clinical implementation," *Br. J. Radiol.*, vol. 87, no. 1034, p. 20130606, Feb. 2014.
- [12] European Society of Radiology (ESR) and American College of Radiology (ACR), "European society of radiology (ESR) and american college of radiology (ACR) report of the 2015 global summit on radiological quality and safety," *Insights Imaging*, vol. 7, no. 4, pp. 481–484, Aug. 2016.
- [13] R. A. Castellino, "Computer aided detection (CAD): an overview," *Cancer Imaging*, vol. 5, no. 1, pp. 17–19, Aug. 2005.
- [14] L. Birnbacher, E.-M. Braig, D. Pfeiffer, F. Pfeiffer, and J. Herzen, "Quantitative x-ray phase contrast computed tomography with grating interferometry : Biomedical applications of quantitative x-ray grating-based phase contrast computed tomography," *Eur. J. Nucl. Med. Mol. Imaging*, vol. 48, no. 13, pp. 4171–4188, Dec. 2021.
- [15] M. Willner, M. Viermetz, M. Marschner, K. Scherer, C. Braun, A. Fingerle, P. Noël, E. Rummeny, F. Pfeiffer, and J. Herzen, "Quantitative three-dimensional imaging of lipid, protein, and water contents via x-ray phase-contrast tomography," *PLoS One*, vol. 11, no. 3, p. e0151889, Mar. 2016.
- [16] H. Ding, M. J. Klopfer, J. L. Ducote, F. Masaki, and S. Molloy, "Breast tissue characterization with photon-counting spectral CT imaging: a postmortem breast study," *Radiology*, vol. 272, no. 3, pp. 731–738, Sep. 2014.
- [17] J. Als-Nielsen and D. McMorrow, "X-rays and their interaction with matter," in *Elements of Modern X-ray Physics*. Wiley, Mar. 2011, pp. 1–28. [Online]. Available: <https://doi.org/10.1002/9781119998365.ch1>
- [18] W. C. Röntgen, "Über eine neue art von strahlen (vorläufige mittheilung)," *Annalen der Physik*, pp. 132–141, Dec. 1895.
- [19] A. Webb and N. B. Smith, *Cambridge texts in biomedical engineering: Introduction to medical imaging: Physics, engineering and clinical applications*. Cambridge, England: Cambridge University Press, Nov. 2010.

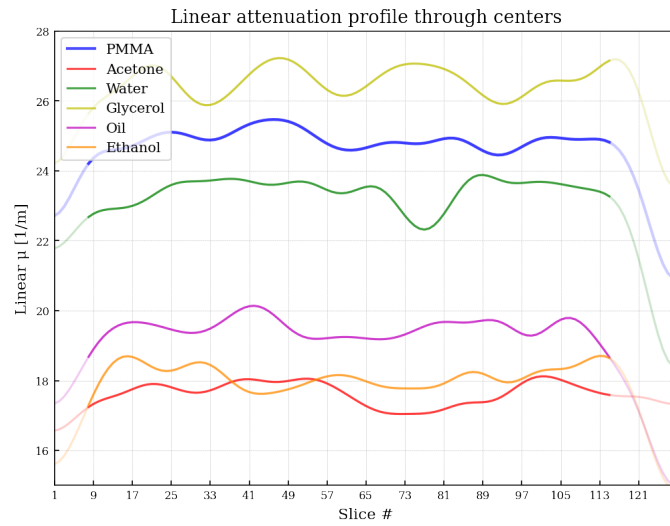
- [20] Beer, "Bestimmung der absorption des rothen lichts in farbigen flüssigkeiten," *Annalen der Physik und Chemie*, vol. 162, no. 5, pp. 78–88, 1852. [Online]. Available: <https://doi.org/10.1002/andp.18521620505>
- [21] P. Sprawls, *Physical principles of medical imaging*, 2nd ed. Madison, WI: Medical Physics Publishing Corporation, Jan. 1995.
- [22] J. D. Bernal, "X-rays in theory and experiment," *Nature*, vol. 136, no. 3443, pp. 661–662, Oct. 1935. [Online]. Available: <https://doi.org/10.1038/136661a0>
- [23] K. Thayalan, "Radiation units and interactions with medium," in *The Physics of Radiology and Imaging*. Jaypee Brothers Medical Publishers (P) Ltd., 2014, pp. 107–107. [Online]. Available: [https://doi.org/10.5005/jp/books/12361\\_5](https://doi.org/10.5005/jp/books/12361_5)
- [24] R. Raupach and T. Flohr, "Performance evaluation of x-ray differential phase contrast computed tomography (PCT) with respect to medical imaging," *Medical Physics*, vol. 39, no. 8, pp. 4761–4774, Jul. 2012. [Online]. Available: <https://doi.org/10.1118/1.4736529>
- [25] U. Bonse and M. Hart, "An X-Ray Interferometer," *Applied Physics Letters*, vol. 6, no. 8, pp. 155–156, Apr. 1965. [Online]. Available: <https://doi.org/10.1063/1.1754212>
- [26] A. Snigirev, I. Snigireva, V. Kohn, S. Kuznetsov, and I. Schelokov, "On the possibilities of x-ray phase contrast microimaging by coherent high-energy synchrotron radiation," *Review of Scientific Instruments*, vol. 66, no. 12, pp. 5486–5492, Dec. 1995. [Online]. Available: <https://doi.org/10.1063/1.1146073>
- [27] M.-C. Zdora, *X-ray Phase-Contrast Imaging Using Near-Field Speckles*. Springer International Publishing, 2021. [Online]. Available: <https://doi.org/10.1007/978-3-030-66329-2>
- [28] T. Weitkamp, A. Diaz, C. David, F. Pfeiffer, M. Stampanoni, P. Cloetens, and E. Ziegler, "X-ray phase imaging with a grating interferometer," *Optics Express*, vol. 13, no. 16, p. 6296, Aug. 2005. [Online]. Available: <https://doi.org/10.1364/opex.13.006296>
- [29] F. Pfeiffer, T. Weitkamp, O. Bunk, and C. David, "Phase retrieval and differential phase-contrast imaging with low-brilliance x-ray sources," *Nature Physics*, vol. 2, no. 4, pp. 258–261, Mar. 2006. [Online]. Available: <https://doi.org/10.1038/nphys265>
- [30] F. Pfeiffer, C. Kottler, O. Bunk, and C. David, "Hard x-ray phase tomography with low-brilliance sources," *Physical Review Letters*, vol. 98, no. 10, Mar. 2007. [Online]. Available: <https://doi.org/10.1103/physrevlett.98.108105>
- [31] J. Vila-Comamala, L. Romano, K. Jefimovs, H. Dejea, A. Bonnin, A. C. Cook, I. Planinc, M. Cikes, Z. Wang, and M. Stampanoni, "High sensitivity x-ray phase

- contrast imaging by laboratory grating-based interferometry at high talbot order geometry," *Optics Express*, vol. 29, no. 2, p. 2049, Jan. 2021. [Online]. Available: <https://doi.org/10.1364/oe.414174>
- [32] J. L. Prince and J. Links, *Medical imaging signals and systems*, 2nd ed. Upper Saddle River, NJ: Pearson, Mar. 2014.
- [33] J. Radon, "Über die Bestimmung von Funktionen durch ihre Integralwerte längs gewisser Mannigfaltigkeiten," *Akad. Wiss.*, vol. 69, pp. 262–277, 1917.
- [34] H. Dejea i Velardo, "Multiscale and dynamic synchrotron-based tomographic microscopy for cardiovascular applications," Ph.D. dissertation, ETH Zürich, 2021.
- [35] F. E. Boas, D. Fleischmann *et al.*, "Ct artifacts: causes and reduction techniques," *Imaging Med*, vol. 4, no. 2, pp. 229–240, 2012.
- [36] C.-C. Cheng, Y.-T. Ching, P.-H. Ko, and Y. Hwu, "Correction of center of rotation and projection angle in synchrotron x-ray computed tomography," *Scientific Reports*, vol. 8, no. 1, Jun. 2018. [Online]. Available: <https://doi.org/10.1038/s41598-018-28149-8>
- [37] J. F. Barrett and N. Keat, "Artifacts in CT: Recognition and avoidance," *RadioGraphics*, vol. 24, no. 6, pp. 1679–1691, Nov. 2004. [Online]. Available: <https://doi.org/10.1148/rg.246045065>
- [38] J. Kiricuta, Ion-Christian and V. Simplăceanu, "Tissue Water Content and Nuclear Magnetic Resonance in Normal and Tumor Tissues," *Cancer Research*, vol. 35, no. 5, pp. 1164–1167, 05 1975.
- [39] K. F. A. Ross and R. E. Gordon, "Water in malignant tissue, measured by cell refractometry and nuclear magnetic resonance," *Journal of Microscopy*, vol. 128, no. 1, pp. 7–21, Oct. 1982. [Online]. Available: <https://doi.org/10.1111/j.1365-2818.1982.tb00433.x>
- [40] A. S. Haka, K. E. Shafer-Peltier, M. Fitzmaurice, J. Crowe, R. R. Dasari, and M. S. Feld, "Diagnosing breast cancer by using raman spectroscopy," *Proceedings of the National Academy of Sciences*, vol. 102, no. 35, pp. 12 371–12 376, Aug. 2005. [Online]. Available: <https://doi.org/10.1073/pnas.0501390102>
- [41] A. M. A. Rømer, M.-L. Thorseth, and D. H. Madsen, "Immune modulatory properties of collagen in cancer," *Frontiers in Immunology*, vol. 12, Dec. 2021. [Online]. Available: <https://doi.org/10.3389/fimmu.2021.791453>
- [42] F. Nassir, R. S. Rector, G. M. Hammoud, and J. A. Ibdah, "Pathogenesis and prevention of hepatic steatosis," *Gastroenterol. Hepatol. (N. Y.)*, vol. 11, no. 3, pp. 167–175, Mar. 2015.

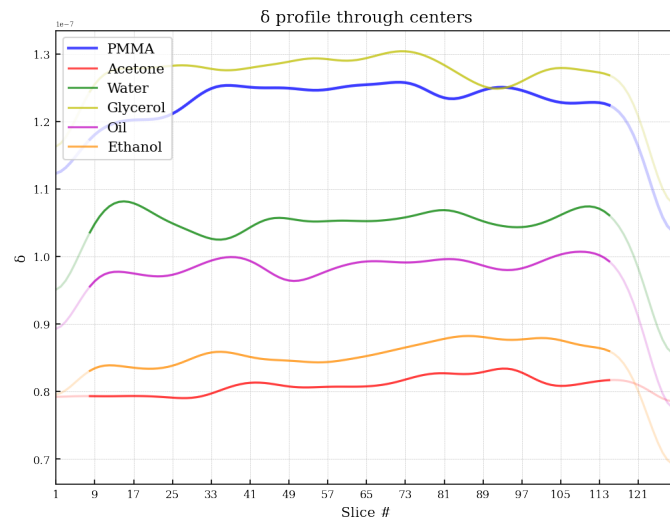
- [43] S. Bellentani, F. Scaglioni, M. Marino, and G. Bedogni, "Epidemiology of non-alcoholic fatty liver disease," *Digestive Diseases*, vol. 28, no. 1, pp. 155–161, 2010. [Online]. Available: <https://doi.org/10.1159/000282080>
- [44] A. O'Sullivan, B. O'Connor, A. Kelly, and M. J. McGrath, "The use of chemical and infrared methods for analysis of milk and dairy products," *International Journal of Dairy Technology*, vol. 52, no. 4, pp. 139–148, Nov. 1999. [Online]. Available: <https://doi.org/10.1111/j.1471-0307.1999.tb02856.x>
- [45] R. E. Alvarez and A. Macovski, "Energy-selective reconstructions in x-ray computerised tomography," *Physics in Medicine and Biology*, vol. 21, no. 5, pp. 733–744, Sep. 1976. [Online]. Available: <https://doi.org/10.1088/0031-9155/21/5/002>
- [46] L. A. Lehmann, R. E. Alvarez, A. Macovski, W. R. Brody, N. J. Pelc, S. J. Riederer, and A. L. Hall, "Generalized image combinations in dual KVP digital radiography," *Medical Physics*, vol. 8, no. 5, pp. 659–667, Sep. 1981. [Online]. Available: <https://doi.org/10.1118/1.595025>
- [47] W. A. Kalender, W. H. Perman, J. R. Vetter, and E. Klotz, "Evaluation of a prototype dual-energy computed tomographic apparatus. i. phantom studies," *Medical Physics*, vol. 13, no. 3, pp. 334–339, May 1986. [Online]. Available: <https://doi.org/10.1118/1.595958>
- [48] B. J. Heismann, J. Leppert, and K. Stierstorfer, "Density and atomic number measurements with spectral x-ray attenuation method," *Journal of Applied Physics*, vol. 94, no. 3, pp. 2073–2079, Aug. 2003. [Online]. Available: <https://doi.org/10.1063/1.1586963>
- [49] X. Liu, L. Yu, A. N. Primak, and C. H. McCollough, "Quantitative imaging of element composition and mass fraction using dual-energy CT: Three-material decomposition," *Medical Physics*, vol. 36, no. 5, pp. 1602–1609, Apr. 2009. [Online]. Available: <https://doi.org/10.1118/1.3097632>
- [50] C. T. Badea, X. Guo, D. Clark, S. M. Johnston, C. D. Marshall, and C. A. Piantadosi, "Dual-energy micro-CT of the rodent lung," *American Journal of Physiology-Lung Cellular and Molecular Physiology*, vol. 302, no. 10, pp. L1088–L1097, May 2012. [Online]. Available: <https://doi.org/10.1152/ajplung.00359.2011>
- [51] P. R. S. Mendonça, P. Lamb, and D. V. Sahani, "A flexible method for multi-material decomposition of dual-energy ct images," *IEEE Transactions on Medical Imaging*, vol. 33, no. 1, pp. 99–116, 2014.
- [52] R. Solem, T. Dreier, I. Goncalves, and M. Bech, "Material decomposition in low-energy micro-CT using a dual-threshold photon counting x-ray detector," *Frontiers in Physics*, vol. 9, May 2021. [Online]. Available: <https://doi.org/10.3389/fphy.2021.673843>

- [53] J. Xu, Z. Wang, S. van Gogh, M. Rawlik, S. Spindler, and M. Stampanoni, "Intensity-based iterative reconstruction for helical grating interferometry breast CT with static grating configuration," *Optics Express*, vol. 30, no. 8, p. 13847, Apr. 2022. [Online]. Available: <https://doi.org/10.1364/oe.455967>
- [54] F. Shahidi, Ed., *Edible Oil and Fat Products: Edible Oils*, 6th ed., ser. Bailey's Industrial Oil and Fat Products. Chichester, England: Wiley-Blackwell, Mar. 2005, vol. 2.
- [55] H. Q. Woodard and D. R. White, "The composition of body tissues," *The British Journal of Radiology*, vol. 59, no. 708, pp. 1209–1218, Dec. 1986. [Online]. Available: <https://doi.org/10.1259/0007-1285-59-708-1209>
- [56] H. Fischer, I. Polikarpov, and A. F. Craievich, "Average protein density is a molecular-weight-dependent function," *Protein Science*, vol. 13, no. 10, pp. 2825–2828, Jan. 2009. [Online]. Available: <https://doi.org/10.1110/ps.04688204>
- [57] D. Micieli, T. Minniti, and G. Gorini, "NeuTomPy toolbox, a python package for tomographic data processing and reconstruction," *SoftwareX*, vol. 9, pp. 260–264, Jan. 2019. [Online]. Available: <https://doi.org/10.1016/j.softx.2019.01.005>
- [58] D. Gürsoy, F. D. Carlo, X. Xiao, and C. Jacobsen, "TomoPy: a framework for the analysis of synchrotron tomographic data," *Journal of Synchrotron Radiation*, vol. 21, no. 5, pp. 1188–1193, Aug. 2014. [Online]. Available: <https://doi.org/10.1107/s1600577514013939>
- [59] W. van Aarle, W. J. Palenstijn, J. Cant, E. Janssens, F. Bleichrodt, A. Dabrovolski, J. D. Beenhouwer, K. J. Batenburg, and J. Sijbers, "Fast and flexible x-ray tomography using the ASTRA toolbox," *Optics Express*, vol. 24, no. 22, p. 25129, Oct. 2016. [Online]. Available: <https://doi.org/10.1364/oe.24.025129>
- [60] S. Seltzer, "Tables of x-ray mass attenuation coefficients and mass energy-absorption coefficients, nist standard reference database 126," 1995. [Online]. Available: <http://www.nist.gov/pml/data/xraycoef/index.cfm>
- [61] L. Kissel, B. Zhou, S. C. Roy, S. K. S. Gupta, and R. H. Pratt, "The validity of form-factor, modified-form-factor and anomalous-scattering-factor approximations in elastic scattering calculations," *Acta Crystallographica Section A Foundations of Crystallography*, vol. 51, no. 3, pp. 271–288, May 1995. [Online]. Available: <https://doi.org/10.1107/s010876739400886x>
- [62] ESRF anonymous FTP server. Accessed: 2022-05-13. [Online]. Available: <http://ftp.esrf.fr/pub/scisoft/xop2.3/DabaxFiles/>

# Supporting results figures

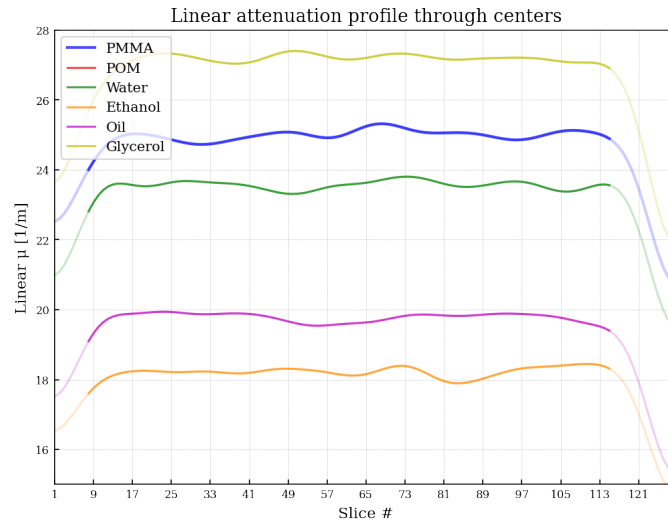


(a) Attenuation coefficients.

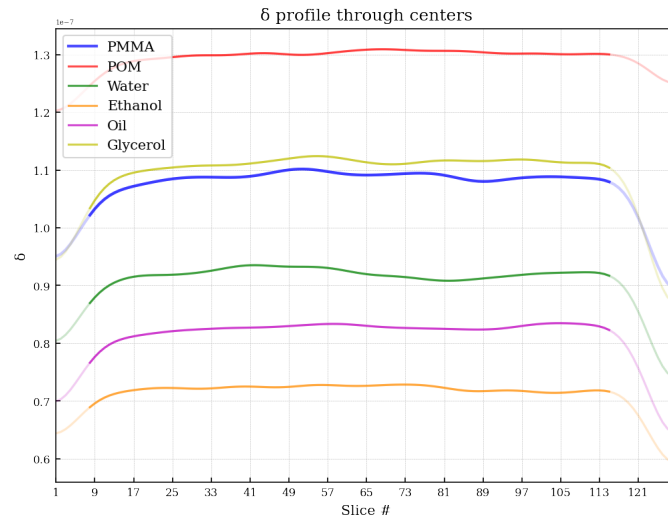


(b) Refractive index decrements.

Fig. A.1. Phantom 1 profile by materials in z-direction, for attenuation coefficients (a) and refractive index decrements (b) after smoothing.

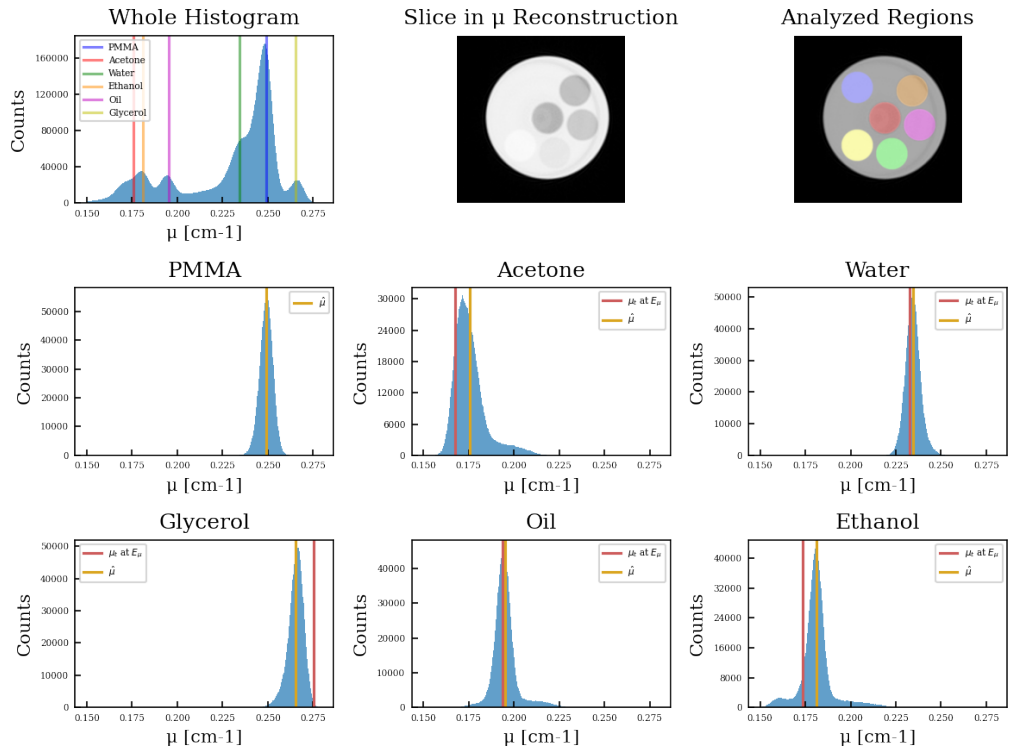


(a) Attenuation coefficients.

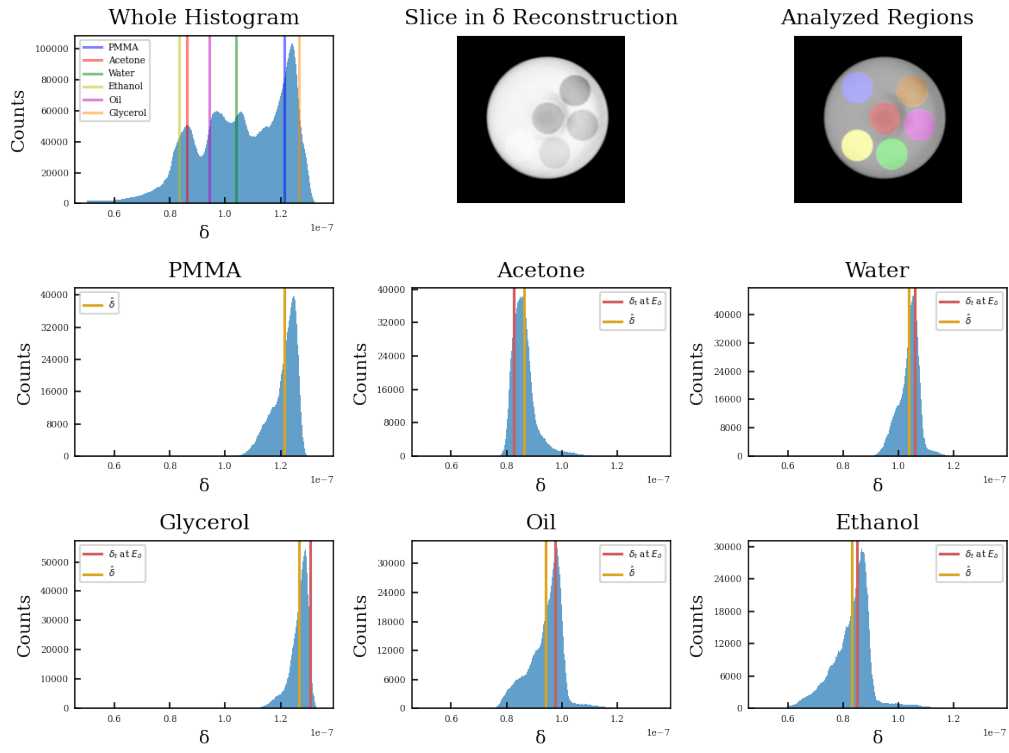


(b) Refractive index decrements.

Fig. A.2. Phantom 2 profile by materials in z-direction, for attenuation coefficients (a) and refractive index decrements (b) after smoothing.



(a) Attenuation coefficients.



(b) Refractive index decrements.

Fig. A.3. Phantom 1 histogram by materials for attenuation coefficients (a) and refractive index decrements (b).

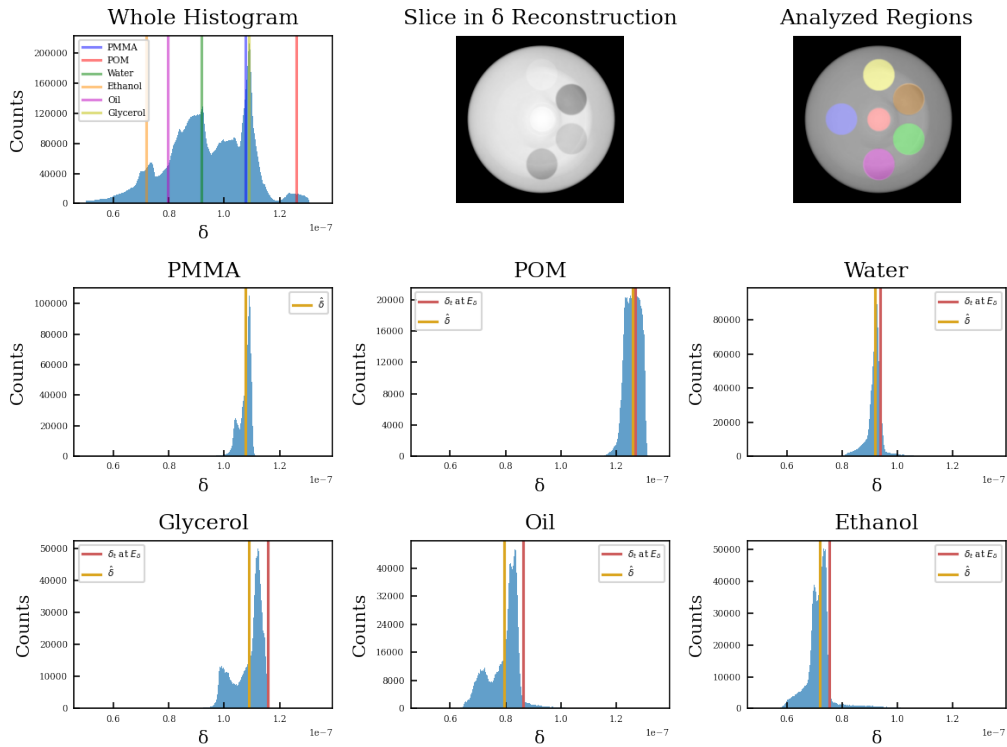
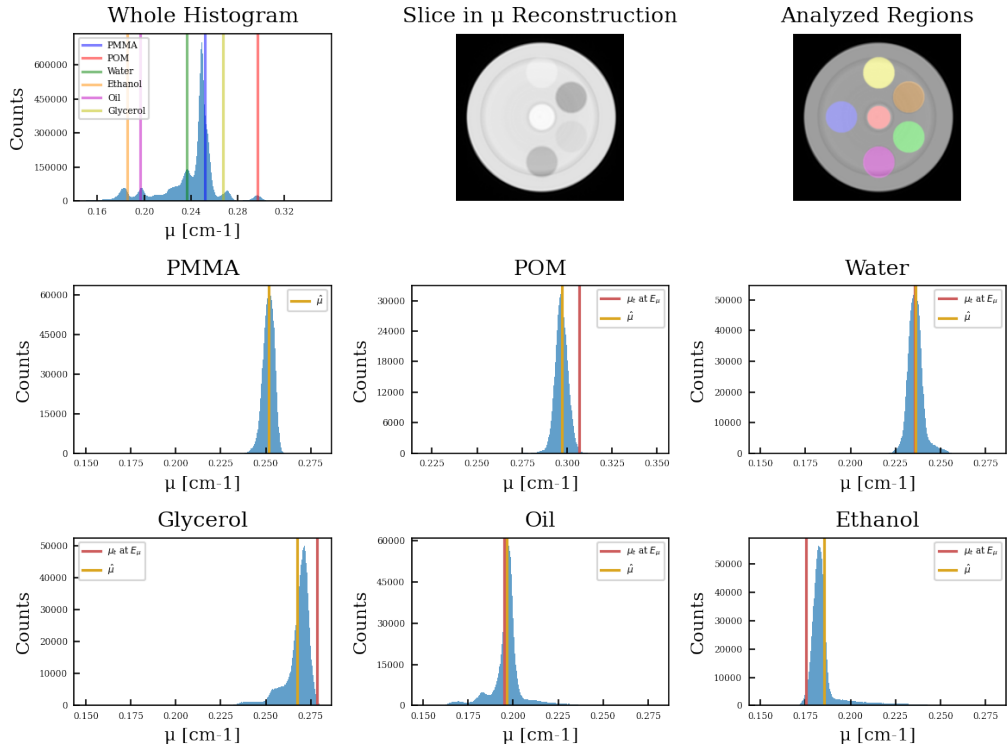


Fig. A.4. Phantom 2 histogram by materials for attenuation coefficients (a) and refractive index decrements (b).

## A.1 Acquisition

## A.2 System assessment

## A.3 Material decomposition

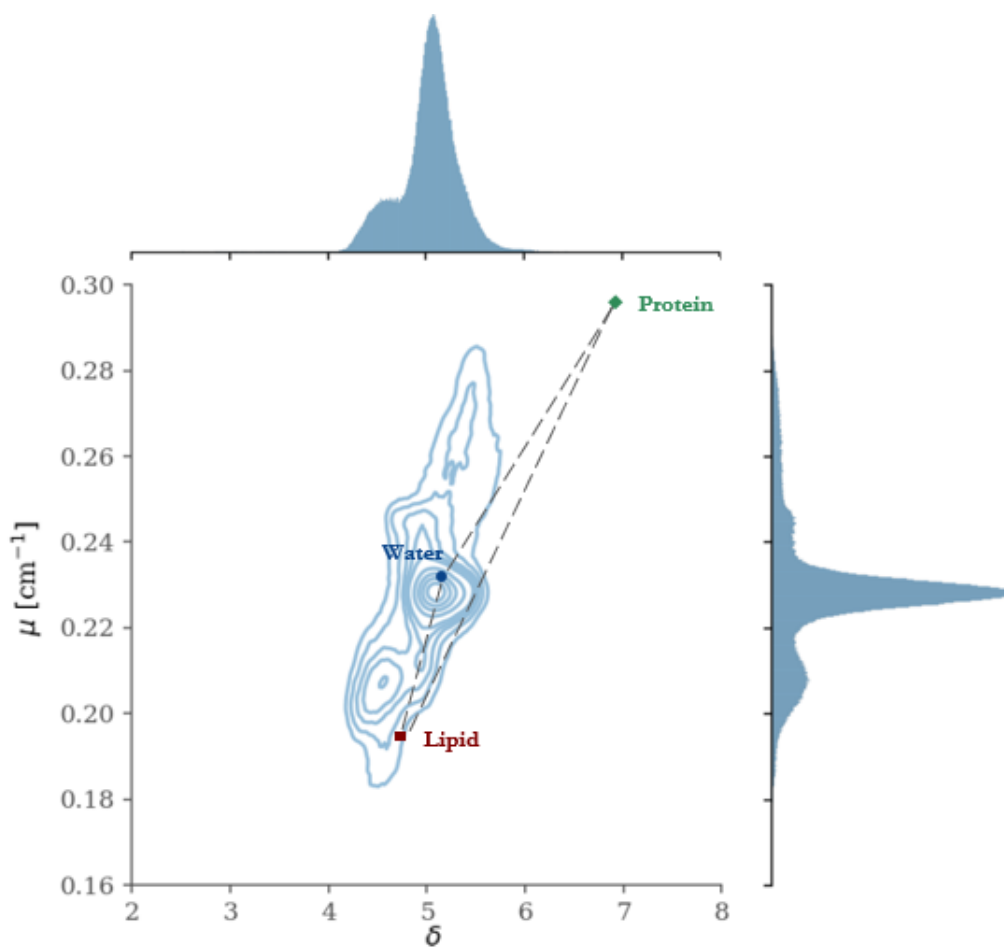


Fig. A.5. Distribution of  $\mu$  and  $\delta$  values in the bacon sample reconstruction. The values found at the effective energies for the basis materials are also represented.